2017

# Towards predicting dry cable galloping using detached eddy simulation

Xingeng Wu
*Iowa State University*

**Towards predicting dry cable galloping using detached eddy simulation**

by

**Xingeng Wu**

A thesis submitted to the graduate faculty

in partial fulfillment of the requirements for the degree of

MASTER OF SCIENCE

Major: Aerospace Engineering

Program of Study Committee:

Anupam Sharma, Co-major Professor

Partha Sarkar, Co-major Professor

Alberto Passalacqua

Iowa State University

Ames, Iowa

2017

# TABLE OF CONTENTS

# LIST OF TABLES

# LIST OF FIGURES

# ACKNOWLEDGEMENTS

I would like to take this opportunity to express my profound gratitude to those who helped me with various aspects of conducting research.

First and foremost, I would like to thank Dr. Anupam Sharma for his guidance, patience and support throughout these two years. His insights and approach to research have often inspired me for doing research during my master's degree studies.

I would also like to thank Dr. Alberto Passalacqua and Dr. Partha Sarkar for kindly serving on the committee. Special thanks to Dr. Partha Sarkar and his student Mohammad Jafari for offering experimental data and Zifei Yin for sharing his turbulence model. I would additionally like to thank my colleagues Bharat, Behnam, Aaron, Andrew, Vishal and Ang, who have shared conversations and guided me on the research.

I would also like to acknowledge the funding from the National Science Foundation (Grant #NSF/CMMI-1537917) and computational resources from the Extreme Science and Engineering Discovery Environment (Grant#TG-CTS130004).

Finally, I must express my very profound gratitude to my parents and to my brother for their constant encouragement and support throughout my master's degree studies. Thank you.

# ABSTRACT

A computational approach based on a $k-\omega$ delayed detached eddy simulation (DDES) model for predicting aerodynamic loads on a smooth circular cylinder (cable) is verified against experiments. Comparisons against preexisting data are performed for a static cylinder where the flow is normal to the cylinder axis. New experiments are conducted where the cylinder axis is inclined with respect to the inflow velocity at the desired yaw angle, $\beta = 30°$. The experimental setup is described and the measurement data is used for code verification. Verification results are presented for two inflow angles, $\beta = 0°$ and $30°$. Comparisons with data include distributions over the cylinder surface of mean and rms of pressure coefficient, mean wake velocity profiles behind the cylinder, and power spectra of sectional lift coefficient.

Simulations are conducted for two general categories - (1) laminar separation, when the laminar boundary layer on the cylinder separates and transition to turbulence occurs in the shear layer, and (2) turbulent separation, when the boundary layer naturally transitions to turbulence, and then the turbulent boundary layer separates. For the laminar separation cases, agreement of predictions with measurements is good for mean and rms surface pressure and wake velocity deficit; the lift spectrum prediction however shows a slight offset in frequency. Very limited experimental data is available in the turbulent separation category.

The results of the three yawed flow cases ($\beta = 15°, 30°, \& 45°$) are found to be independent of $\beta$ (dynamic scaling) when the flow speed normal to the cylinder axis is selected as the reference velocity scale. This 'independence' is observed when the category of flow separation does not change with $\beta$. Spatio-temporal plots of instantaneous sectional lift and drag for yawed flow simulations clearly show presence of spanwise flow.

Finally, the capability of the solver to perform dynamic simulations is demonstrated for two canonical, prescribed cylinder motions - transverse and horizontal harmonic oscillations for a given frequency and amplitude. The mean and unsteady loads on the cylinder are found to

vary drastically with cylinder motion. The results and verification with experiments presented here demonstrate the capability of the computational methodology to accurately predict aerodynamic loading on cables. Accurate load prediction is a critical element in aeroelastic models that are required to predict dry cable galloping.

# CHAPTER 1. INTRODUCTION

The primary goal of this thesis is to develop computational methodology to predict wind load on cables with the ultimate objective of improving the resilience of cables, used in cable-supported structures and high-voltage power transmission lines, to hazards posed by moderate to extreme wind. Cables are often used in groups/bundles in a variety of engineering applications such as in bridges (cable-stayed, suspension, and tied-arch), suspended roofs, guyed lattice towers, and for power transmission. These cables, particularly the longer ones, are prone to large-amplitude vibrations in wind due to their low inherent structural damping ($< 0.5\%$). The vibration mechanisms involve complex aeroelastic (motion-induced) interactions that depend on the spatial orientation, geometry, surface-characteristics, and dynamic properties of cables. Large amplitude vibrations can lead to either catastrophic- or fatigue failure of the cables and/or the adjoining structure, which poses a significant threat to the safety and serviceability of these systems. Such damage inducing conditions arise in wind alone and in wind with precipitation (rain or ice). The different kinds of cable vibrations are briefly explained next and their key properties are summarized in Table 1.1. Vortex Induced Vibration (VIV) occurs when the vortex shedding frequency ($f = U\ St/D$) locks-in with the natural structural frequency of the cable. The oscillation amplitude is inversely related to the Scruton number, $S_c = m\zeta/(\rho D^2)$, where $\zeta$ is the critical damping ratio. Karman-vortex-induced excitation does not pose a significant threat to cables since it causes relatively low amplitudes of vibration and occurs at relatively low wind speeds ($< 10$ m/s).

Rain-Wind Induced Vibration (RWIV) is a large-amplitude, low frequency vibration that occurs when inclined (and yawed) cables are simultaneously exposed to rain and wind. It has been observed on multiple cable-stayed bridges (Matsumoto et al., 1995; Phelan et al., 2006) and is caused due to a water rivulet on the upper surface of a cable that makes the cable

Table 1.1: Summary of classifications of cable vibrations with key properties

| | **Inclined cables** (e.g., staycables) | **Horizontally-spanned cables** (e.g., power conductors) |
|---|---|---|
| ***Vortex Induced Vibration (VIV)*** | All cables<br>• $A < 0.02\ D$<br>• Low wind<br>• No concern for small diameter cables | All conductors<br>• $f = 3 - 150$<br>• $A = 0.01 - 1\ D$<br>• $U = 1 - 7$ m/s<br>• Bare or uniform ice |
| ***Rain-Wind Induced Vibration (RWIV)*** | Few cables<br>• Large A<br>• $U \sim 4 - 18\ m/s$<br>• Rain with yawed wind<br>• Concern | Not observed |
| ***Galloping*** | Few cables<br>• Large A<br>• High wind<br>• Bare cable with yawed wind<br>• Concern | All cables<br>• $f = 0.08 - 3$<br>• $A = 5 - 300\ D$, steady<br>• $U = 7 - 18$ m/s<br>• Asymmetric ice deposit, high loads |
| ***Wake Galloping*** | All cables | Bundled conductors<br>• $f = 0.15 - 10$<br>• $A = 0.5 - 80\ D$, steady<br>• Bare conductor clashing → wear |

***Key:*** *A, peak-to-peak amplitudes; D, cable diameter; f, frequency in Hz; U, wind velocity*

cross-section asymmetric(Hikami and Shiraishi, 1988). The inherent low structural damping ratio of cable stays in transverse oscillation is easily overcome by the aerodynamic excitation, leading to RWIV.

Galloping is an aerodynamic instability characterized by low-frequency, large-amplitude oscillations of cables normal to the wind direction. The galloping phenomenon was first observed by Davison (1930) for ice/sleet coated power conductors and explained by Den Hartog (1932) as caused due to an aerodynamic instability. The Glauert-Den Hartog criterion ($dC_l/d\alpha + C_d < 0$) marks the incipience of galloping instability. For cables with circular cross-sections in normally-incident wind, $dC_l/d\alpha = 0$ and $C_d > 0$, therefore galloping instability should not occur. However, accumulation of ice on these conductors makes the cable cross-section asymmetric. This asymmetry can render the aerodynamic lift curve to have a negative slope and trigger galloping instability.

While researches by Rawlins (1981), Den Hartog (1985) and Yukino et al. (1995) suggest galloping of transmission lines appears to occur primarily due to ice accretion, galloping has also been observed under no-ice conditions by Davis et al. (1963). According to Matsumoto et al. (2010, 1990), dry inclined cable galloping, often referred as dry cable vibration, can occur for inclined circular cables (e.g., stay cables) at high wind speeds even when the cross section remains axisymmetric. The cause of this instability is understood to be the asymmetry in the flow because of the relative yaw between the cable- and wind directions. The development of flow along the cable axis favors dry cable vibration. In bare conductors, the grooves in the cables can affect this axial flow and hence the instability.

Wake galloping instability is observed in groups of cables, such as in bundled conductors (Cigada et al., 1997) or in cable-stayed bridges (Yoshimura et al., 1995), because of mutual aerodynamic interference. A criterion to describe the onset of the wake galloping instability (Irwin, 1997) has been proposed – the instability is triggered when the wind speed exceeds $U_{crit} = c_0\ f_n D\sqrt{Sc}$, where $c_0$ is a constant that depends on inter-cable spacing and orientation, $f_n$ is a natural frequency, $D$ is the cable diameter, and $Sc$ is the Scruton number.

The RMIV and VIV phenomena are restricted to low wind speeds ($< 20$ m/s) and have been extensively studied. In contrast, "wake galloping" and "galloping or dry-cable vibration" have not been adequately researched. Past investigations of wind-cable interaction based on wind tunnel tests and a handful of CFD studies have been largely restricted to individual cables with smooth surface (stay cables) and vibrating in a single vertical plane in wind flow that is smooth, stationary and uniform. These studies spanning over at least three decades have resulted in an improved understanding of the cause of these vibrations, particularly the RWIV phenomenon. However, there exist discrepancies in different criteria for dry-cable galloping instabilities between different model studies of inclined cables, possibly because of limited number of studies and oversimplification of the problem. This thesis focuses on the dry-cable galloping problem and presents results of our process towards the goal of developing an aeroelastic load model for dry-cable galloping.

The following section gives a brief overview of the computational methodology used in this study.

## 1.1 Computational Methodology

In fluid dynamics, for a flow passing through fixed control volume, the continuity equation can be written as

$$\frac{\partial \rho}{\partial t} + \boldsymbol{\nabla} \cdot (\rho \boldsymbol{U}) = 0, \tag{1.1}$$

where $\rho$ is fluid density, $t$ is time and $\boldsymbol{U}$ is flow velocity. The first term in Eq. 1.1 is the change in fluid density in the control volume per unit time. The second term is the rate of mass flux passing out of the control surface per unit time. Hence, the continuity equation presents the law of conservation of mass. This equation can be written in non-conservation form as

$$\frac{D\rho}{Dt} + \rho(\boldsymbol{\nabla} \cdot \boldsymbol{U}) = 0, \tag{1.2}$$

where $D/Dt$ is the material derivative. Since the flow Mach number in the problem under investigation is less than 0.2, the flow is approximated to be incompressible. In this case, since $\rho$ =constant, $D\rho/Dt = 0$, which simplifies Eq. 1.2 to

$$\boldsymbol{\nabla} \cdot \boldsymbol{U} = 0.$$

This equation can be written using indicial notation as

$$\frac{\partial U_i}{\partial x_i} = 0. \tag{1.3}$$

Another governing equation for incompressible flow is the momentum equation, which can be written as

$$\frac{DU_i}{Dt} = -\frac{1}{\rho}\frac{\partial P}{\partial x_i} + \frac{\tau_{ij}}{\partial x_j}, \tag{1.4}$$

where $P$ is the pressure and $\tau_{ij}$ is the stress tensor, defined as

$$\tau_{ij} = \nu(\frac{\partial U_i}{\partial x_j} + \frac{\partial U_j}{\partial x_i}) = 2\nu S_{ij},$$

where $\nu$ is kinematic viscosity, $S_{ij}$ is the strain rate tensor.

Incompressible turbulent flow is governed by Eqs. 1.3 and 1.4. However, in large eddy simulation (LES) and detached eddy simulation (DES) models, the equations are spatially filtered (low-pass) and the numerical procedure solves for the filtered quantities that can be

resolved by the grid. The sub-filter (or sub-grid) quantities exert a "stress" on the filtered flow-field, which is modeled using a sub-grid scale (SGS) stress model. A common filtering operation of separating filtered and sub-filter quantity is

$$A = \tilde{A} + a,$$

where A can represent any quantity that can be filtered, $\tilde{A}$ is the spatially filtered quantity and $a$ is the sub-filter quantity. After applying the filtering operation, the governing equations of incompressible flow with an eddy-viscosity turbulence model become

$$\frac{\partial \tilde{U}_i}{\partial x_i} = 0, \; and$$
$$\frac{\partial \tilde{U}_i}{\partial t} + \frac{\partial (\tilde{U}_j \tilde{U}_i)}{\partial x_j} = -\frac{1}{\rho}\frac{\partial \tilde{p}}{\partial x_i} + \nu \frac{\partial^2 \tilde{U}_i}{\partial x_j^2} - \frac{\partial \tau_{ij}}{\partial x_j},$$

where $\tau_{ij} = \widetilde{U_i U_j} - \tilde{U}_i \tilde{U}_j = -2\,\nu_{SGS}\,\tilde{S}$ and $\tilde{S} = (\partial \tilde{U}_i/\partial x_j + \partial \tilde{U}_j/\partial x_i)/2$. In the above, SGS denotes a sub-grid scale quantity, $\tau_{ij}^{SGS}$ denotes the sub-grid scale stress tensor which is modeled as the product of eddy viscosity, $\nu_{SGS}$ and the strain rate tensor $S_{ij}$; turbulence models of such type are referred to as eddy-viscosity models. Further details about the turbulence model are described in Chapter 2.

The remainder of the thesis is organized as follows:

Chapter 2 is a paper that was presented at the 2017 AIAA SciTech Forum and is being submitted to the journal Engineering Structures for archival publication. It describes in detail the computational methodology, the experiments conducted, and verification results. Chapter 3 presents the conclusion drawn from this study and presents some prospects for future work in the area.

# CHAPTER 2. TOWARDS PREDICTING DRY CABLE GALLOPING USING DETACHED EDDY SIMULATION

Xingeng Wu, Mohammad Jafari, Partha Sarkar, Anupam Sharma

**Engineering Structures: Submitted**

A computational approach based on a $k-\omega$ delayed detached eddy simulation (DDES) model for predicting aerodynamic loads on a smooth circular cylinder (cable) is verified against experiments. Comparisons against preexisting data are performed for a static cylinder where the flow is normal to the cylinder axis. New experiments are conducted where the cylinder axis is inclined with respect to the inflow velocity at the desired yaw angle, $\beta = 30°$. The experimental setup is described and the measurement data is used for code verification. Verification results are presented for two inflow angles, $\beta = 0°$ and $30°$. Comparisons with data include distributions over the cylinder surface of mean and rms of pressure coefficient, mean wake velocity profiles behind the cylinder, and power spectra of sectional lift coefficient.

Simulations are conducted for two general categories - (1) laminar separation, when the laminar boundary layer on the cylinder separates and transition to turbulence occurs in the shear layer, and (2) turbulent separation, when the boundary layer naturally transitions to turbulent, and then the turbulent boundary layer separates. For the laminar separation cases, agreement of predictions with measurements is good for mean and rms surface pressure and wake velocity deficit; the lift spectrum prediction however shows a slight offset in frequency. Very limited experimental data is available in the turbulent separation category.

The results of the three yawed flow cases ($\beta = 15°, 30°,$ & $45°$) are found to be independent of $\beta$ (dynamic scaling) when the flow speed normal to the cylinder axis is selected as the reference velocity scale. This 'independence' is observed when the category of flow separation

does not change with $\beta$. Spatio-temporal plots of instantaneous sectional lift and drag for yawed flow simulations clearly show presence of spanwise flow.

Finally, the capability of the solver to perform dynamic simulations is demonstrated for two canonical, prescribed cylinder motions - transverse and horizontal harmonic oscillations for a given frequency and amplitude. The mean and unsteady loads on the cylinder are found to vary drastically with cylinder motion. The results and verification with experiments presented here demonstrate the capability of the computational methodology to accurately predict aerodynamic loading on cables. Accurate load prediction is a critical element in aeroelastic models that are required to predict dry cable galloping.

## 2.1 Introduction

Inclined and horizontally- or vertically-spanned cables are used in various engineering applications: cable-stayed, suspension, and tied-arch bridges, power transmission lines, guyed lattice towers, suspension roofs etc. These cables (particularly long cables) are prone to large-amplitude wind-induced vibration, due to their low inherent structural damping ($< 0.5\%$), which can lead to catastrophic failure of the cables and the structures supported by them. The vibration mechanisms involve complex aeroelastic (motion-induced) interactions that depend on the spatial orientation, geometry, surface-characteristics, and dynamic properties of cables. Davenport (1995) shows that large amplitude vibrations can lead to either catastrophic- or fatigue failure of the cables and/or the adjoining structure, which poses a significant threat to the safety and serviceability of these systems.

Galloping is an aerodynamic instability characterized by low-frequency, large-amplitude oscillations of cables normal to the wind direction. The galloping phenomenon was first observed by Davison (1930) for ice/sleet coated power conductors and explained by Den Hartog (1932) as caused due to an aerodynamic instability. The Glauert-Den Hartog criterion ($dC_l/d\alpha + C_d < 0$) marks the incipience of galloping instability. For circular cables in normally-incident wind, $dC_l/d\alpha = 0$ and $C_d > 0$, therefore galloping instability should not occur. However, accumulation of ice on these conductors makes the cable cross-section asymmetric. This asymmetry can render the aerodynamic lift curve to have a negative slope and trigger galloping instability.

While researches by Rawlins (1981), Den Hartog (1985) and Yukino et al. (1995) suggest galloping of transmission lines appears to occur primarily due to ice accretion, galloping has also been observed under no-ice conditions by Davis et al. (1963). According to Matsumoto et al. (2010, 1990), dry inclined cable galloping, often referred as dry cable vibration, can occur for inclined circular cables (e.g., stay cables) at high wind speeds even when the cross section remains axisymmetric. The cause of this instability is understood to be the asymmetry in the flow because of the relative yaw between the cable- and wind directions. The development of flow along the cable axis favors dry cable vibration. In bare conductors, the grooves in the cables can affect this axial flow and hence the instability.

A criterion to describe the onset of divergent response of dry cable vibration has been proposed – the instability is triggered when the wind speed exceeds, $U_{cr} = c\, f_n\, D\, Sc^p$, where $c$ and $p$ are constants, $f_n$ is a natural frequency, $D$ is the cable diameter, and $Sc$ is the Scruton number; the constants $c = 35,\ p = 2/3$ per Honda et al. (1995) and $c = 35,\ p = 1/2$ per Irwin (1997). The criterion by Irwin (1997) for the onset of velocity is quite conservative, i.e., it gives lower critical values of $U$ than the criterion by Honda et al. (1995). Another study by Cheng et al. (2003) gives value of $U_{cr}$ lower than that given by either Honda et al. (1995) or Irwin (1997). The critical velocity for divergent response of a single degree-of-freedom (DOF) section model of a yawed cylinder by Sarkar et al. (1998) for $Sc = 0.6$, and for a two-DOF section model of a yawed cylinder by Sarkar and Gardner (2000) for $Sc = 2.5$ were greater than that calculated using Honda et al. (1995) with the corresponding $Sc$. Thus, discrepancies exist between different criteria and studies for incipience of instability or divergent motions. Further, it is difficult to validate these criteria because of limited field data sets of cable response at wind speeds $> 15$ m/s when dry-cable vibration can occur.

Past investigations of wind-cable dynamic interaction, with and without precipitation, were based primarily on wind tunnel tests and a limited number of CFD and field studies. These studies, spanning over the past three decades, have resulted in an improved understanding of the cause of these vibrations, particularly the rain-wind induced vibration phenomenon, which is restricted to a small range of wind speeds ($8 - 15$ m/s) (Kumarasena et al., 2005). Only a limited number of studies of cable aerodynamics have been performed till date at moderate to

high wind speeds where large-amplitude vibration (velocity restricted or divergent) can occur. There is a clear need for an accurate aerodynamic/aeroelastic load model that can be used to predict the dynamic response of dry- or iced-cables in turbulent/transient wind associated with extreme wind hazards.

This paper presents results of our progress towards the goal of developing an aeroelastic load model for dry-cable vibration. The objective is to be able to accurately predict aerodynamic loading on a single, smooth circular cylinder operating in smooth inflow (normal and yawed flow) for static and dynamic conditions. This paper focuses on verifying the computational methodology against experimental data for normally-incident flow and yawed flow. The capability of the solver to predict loads when the cylinder is in prescribed motion is also demonstrated for two canonical vibration cases. To our knowledge, this is the first attempt at investigating dry-cable galloping using delayed detached eddy Simulations (DDES) with extensive verification against existing experimental data as well new experiments which form a part of this paper.

## 2.2 Computational Methodology

The flow is approximated to be incompressible since the flow Mach number is less than 0.2. Various degrees of approximations can be utilized to model flow turbulence: from resolving only time-averaged quantities in Reynolds Averaged Navier-Stokes or RANS, to resolving the tiniest of turbulent eddies in Direct Numerical Simulations or DNS. Large eddy simulations (LES) resolve energy containing eddies but model the net effect of smaller (unresolved/universal) eddies on larger (resolved) eddies. The detached eddy simulation (DES) technique (Spalart et al., 1997) is a hybrid approach that uses RANS equations to simulate attached flow near solid surfaces and LES for separated (detached) flow away from the surfaces. DES allows computation of high Reynolds number flows relatively inexpensively by removing the constraint in LES to have very fine grids near solid boundaries.

Flow over slender structures with circular cross-section has been studied using unsteady RANS (Pontaza et al., 2009), DES (Travin et al., 2000; Yeo and Jones, 2012), LES (Breuer, 1998; Kravchenko and Moin, 2000; Catalano et al., 2003), and DNS (Dong and Karniadakis,

2005; Zhao et al., 2009) approaches. Latest numerical efforts in simulating aerodynamics of cable vibration have utilized DES (Yeo et al., 2007; Yeo and Jones, 2008, 2012, 2011) as the primary numerical approach. Detailed flow simulations have been performed with a single, stationary, yawed cylinder in uniform inflow (Yeo et al., 2007; Yeo and Jones, 2008) and oscillating inflow (Yeo and Jones, 2012). It has been concluded by Yeo and Jones (2012) that oblique wind-induced aerodynamic forces play an important role in initiating and increasing the vibration at low frequencies. DES has also been used to investigate the use of strakes in cables for aerodynamic mitigation of wind-induced oscillations by Yeo and Jones (2011). In essence, high-fidelity simulations have been instrumental in gaining insights into the problem of wind-induced cable vibration.

In LES and DES, the equations are spatially filtered (low-pass) and the numerical procedure solves for the filtered quantities that can be resolved by the grid. The sub-filter (or sub-grid) quantities exert a "stress" on the filtered flow-field, which is modeled using a sub-grid scale (SGS) stress model. Denoting spatially filtered quantities by overhead tilde (~), the incompressible flow equations with an eddy-viscosity turbulence model are

$$\frac{\partial \tilde{U}_i}{\partial x_i} = 0, \ and$$
$$\frac{\partial \tilde{U}_i}{\partial t} + \frac{\partial (\tilde{U}_j \tilde{U}_i)}{\partial x_j} = -\frac{1}{\rho}\frac{\partial \tilde{p}}{\partial x_i} + \nu \frac{\partial^2 \tilde{U}_i}{\partial x_j^2} - \frac{\partial \tau_{ij}}{\partial x_j},$$

where $\tau_{ij} = \widetilde{U_i U_j} - \tilde{U}_i \tilde{U}_j = -2\,\nu_{SGS}\,\tilde{S}$ and $\tilde{S} = (\partial \tilde{U}_i/\partial x_j + \partial \tilde{U}_j/\partial x_i)/2$. In the above, SGS denotes a sub-grid scale quantity, $\tau_{ij}^{SGS}$ denotes the sub-grid scale stress tensor which is modeled as the product of eddy viscosity, $\nu_{SGS}$ and the strain rate tensor $S_{ij}$; turbulence models of such type are referred to as eddy-viscosity models. DES is a non-zonal hybrid RANS-LES method, where a RANS turbulence model is used to compute the eddy viscosity for the SGS stress tensor in the corresponding LES. In the original DES formulation (Spalart et al. (1997)), the Spalart-Allamaras (SA) LES and SA-RANS models were used. We use the method developed by Yin et al. (2015), which introduces a dynamic procedure to improve the DES capability by correcting for modeled stress depletion and log-layer mismatch. This model has been implemented in the open source CFD software OpenFOAM. All the simulations in this paper are obtained using OpenFOAM. The numerical scheme uses second order backward difference for time integration

and linear interpolation with central differencing for spatial discretization of the governing equations.

### 2.2.1 Detached Eddy Simulation Model

A summary of the DES model used in this study is provided here; details are available in Yin et al. (2015). It uses a $k-\omega$ turbulence closure model in the RANS zones, and the same model is used to calculate $\nu_T$ in the LES zones. The eddy viscosity in the $k-\omega$ DDES can be defined as $\nu_T = l_{DDES}^2\,\omega$, where $l_{DDES}$ is the DDES length scale. The different length scales in the $k-\omega$ DDES model are defined as

$$
\begin{aligned}
l_{DDES} &= l_{RANS} - f_d\,\max\left(0, l_{RANS} - l_{LES}\right),\\
l_{RANS} &= \sqrt{k}/\omega,\\
l_{LES} &= C_{DES}\triangle,\\
\triangle &= f_d\,V^{1/3} + (1-f_d)\,h_{max},\\
\nu_T &= l_{DDES}^2\,\omega,
\end{aligned}
$$

where, $l_{RANS}$ and $l_{LES}$ are the length scales of the RANS and LES branches respectively, $h_{max} = \max(dx, dy, dz)$ is the maximum grid size, and $f_d$ is a shielding function of the DDES model, defined as $f_d = 1 - \tanh\{(8\,r_d)^3\}$, where

$$
r_d = \frac{k/\omega + \nu}{\kappa^2\,d_w^2\,\sqrt{U_{i,j}U_{i,j}}};
$$

$\nu$ is the molecular viscosity, $\kappa$ is the von Karman constant, $d_w$ is the distance between the cell and the nearest wall, and $U_{i,j} = \partial_j U_i$ is the velocity gradient. In the RANS branch, the transport equation for k and $\omega$ are written as

$$
\begin{aligned}
\frac{Dk}{Dt} &= 2\nu_T|S|^2 - C_\mu k\omega + \partial_j[(\nu + \sigma_k\nu_T)\partial_j k],\\
\frac{D\omega}{Dt} &= 2C_{\omega 1}|S|^2 - C_{\omega 2}\omega^2 + \partial_j[(\nu + \sigma_\omega\nu_T)\partial_j\omega],\ \text{where } \nu_{\mathrm{T}} = \mathrm{k}^2/\omega.
\end{aligned}
$$

In the LES region ($f_d = 1, l_{DDES} = C_{DES}\,\triangle$), the eddy viscosity switches to $\nu_T = l_{DDES}^2\,\omega = (C_{DES}\triangle)^2\omega$, which is similar to the eddy viscosity in the Smagorinsky model, $\nu_s = (C_s\triangle)^2|S|$.

The LES branch of this $k-\omega$ DDES model uses a dynamic procedure which defines the value of $C_{DES}$ as

$$
\begin{aligned}
C_{DES} &= \max\left(C_{lim}, C_{dyn}\right), \\
C_{dyn}^2 &= \max\left(0,\ 0.5\frac{L_{i,j}M_{i,j}}{M_{i,j}M_{i,j}}\right), \\
C_{lim} &= C_{DES}^0\left[1-\tanh\left(\alpha\exp\left(\frac{-\beta\, h_{max}}{L_k}\right)\right)\right], \\
C_{DES}^0 &= 0.12, \quad L_k = \left(\frac{\nu^3}{\epsilon}\right)^{\frac{1}{4}}, \quad \alpha = 25, \quad \beta = 0.05, \\
\epsilon &= 2\left(C_{DES}^0 h_{max}\right)^2\omega\left|S\right|^2 + C_\mu k\,\omega.
\end{aligned}
$$

For further details about the DES model, the reader is referred to Yin et al. (2015).

### 2.2.2 Computational Grids

The outer boundary of the computational domain is circular with a radius of $25\times D$, where $D$ is the diameter of the cylinder. The cylinder is placed in the center of the domain. The span dimension is $2\times D$ for normal-cylinder (flow normal to cylinder axis) cases and $10\times D$ for inclined-cylinder (flow at an angle to cylinder axis) cases Periodic boundary conditions are used in the span direction, while freestream condition is used on the outer radial boundary. The domain is discretized using a multi-block grid that has three blocks: (1) an O-grid is used to resolve the flow around the cylinder, (2) an H-grid to resolve the wake, and (3) a C-grid for the far field. In order to accurately capture the aerodynamic forces on the cylinder, the flow around the cylinder and in the near-wake region has to be resolved with high precision. A fine mesh is therefore applied in these regions. Figure 2.1 shows a cross-sectional view of the full computational domain as well as a zoom-view to highlight grid topology.

## 2.3 Experimental Setup and Measurements

Static wind tunnel experiments were conducted on a smooth cylinder of circular cross section representing a stay cable to measure the aerodynamic forces and the velocity distribution in its wake. These experiments were performed in the Aerodynamic/Atmospheric Boundary Layer

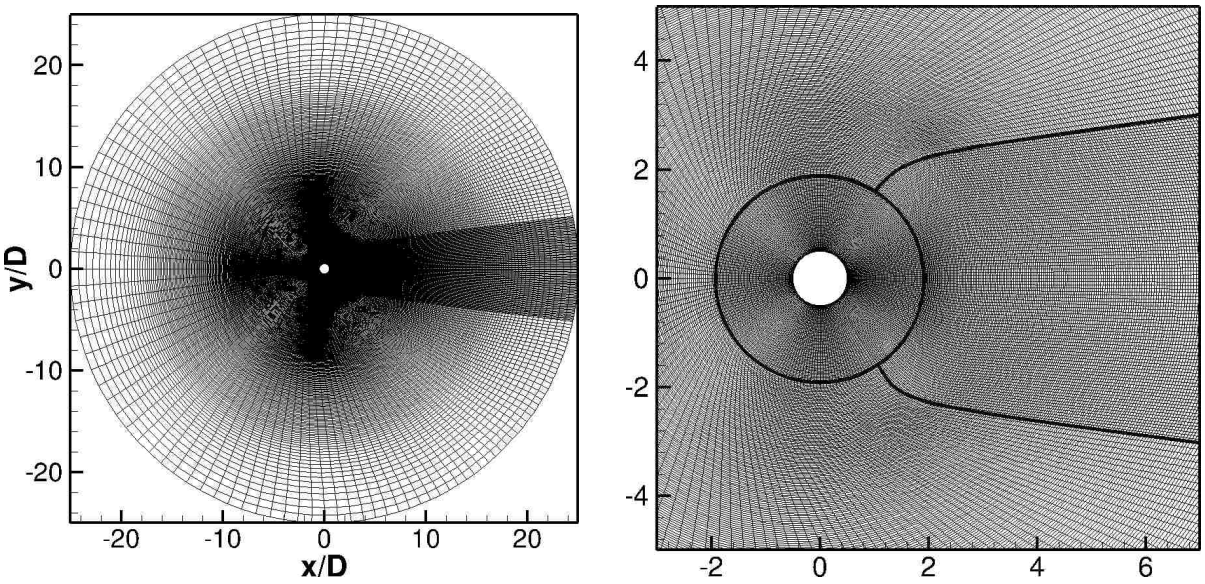


(a) Overall CFD domain

(b) Zoom view of near-cylinder mesh

Figure 2.1: Cross-sectional views of the computational grid

(AABL) Wind and Gust Tunnel located in the Department of Aerospace Engineering at Iowa State University. This wind tunnel has an aerodynamic test section of 2.44 m (8.0 ft) width × 1.83 m (6.0 ft) height and a design maximum wind speed of 53 m/s (173.9 ft/s). A polished aluminum tube with diameter, $D = 0.127$ m and length, $L = 1.52$ m was selected as the smooth cylinder model. Although the aspect ratio ($L/D = 12$) is enough to prevent edge effects in a circular cylinder, two circular plates of diameter $4\,D$ were attached to the ends of the cylinder. These plates were adjusted for each cylinder yaw angle to be parallel to the incoming airflow to ensure 2D flow over the cylinder. The blockage ratio in the tunnel with the model was approximately 5% for all measurements. Figure 2.2 displays the model setup in the AABL tunnel with the cylinder in normal-flow and yawed-flow configurations. An innovative multi-functional static setup was designed to measure the pressure distribution and velocity profile for different yaw angles. As shown in Fig. 2.2, this setup properly secures the model for different yaw angles.

As seen in Fig. 2.3, the model has 128 pressure taps distributed on its surface to measure local, instantaneous pressure. These pressure values are used to compute aerodynamic lift and drag (viscous part ignored) on the cylinder as well as pressure correlations along the span.


(a) setup for normal-flow measurements


(b) setup for yawed flow measurements

Figure 2.2: Pictures showing the model setup used to allow measurements at arbitrary inflow angles. The Cobra probe used to measure the wake is shown in (a).

There are 36 pressure taps at equal angular spacing of 10 degrees along each of the three rings located on the cylinder. The three rings are labeled Right (R), Middle (M), and Left (L) as seen in Fig. 2.3 (a) and are spaced $4D$ and $5D$ apart from each other along the span. Another set of pressure taps are located at a fixed angular location at equal spacing of $1D$ along the span between the rings (see Fig. 2.3 (a,b)).

### 2.3.1 Data Acquisition System

For wake measurement, one Cobra Probe (4-hole velocity probe) mounted on a traverse system was used to measure the velocity field behind the model (see Fig. 2.2 (a)). In order to minimize the blockage effect of the traverse system, its cross section was streamlined by using an airfoil section. For velocity measurements, the sampling rate was 1250 Hz and the sampling time was 60 s. Wake measurement were made $2.5D$ downstream of the model (measured from the cylinder axis), where the turbulence intensity was lower than the maximum allowable intensity (overall 30%) for the Cobra probe.

Two 64-channel pressure modules (Scanivalve ZOC 33/64 Px) were utilized to capture the local pressure. In addition, an Ethernet remote A/D system (ERAD) was used as a collection system to read information from the ZOC. The sampling rate and sampling time for all pressure measurements were 250 Hz and 60 s respectively. The Scantel program from Scanivalve was

used for pressure data acquisition. In order to minimize the error of measurement due to the tube length, both ZOCs were placed inside the wind tunnel near the model (Fig. 2.2 (b)). The wake measurement traverse system was removed when surface pressure measurements were made.

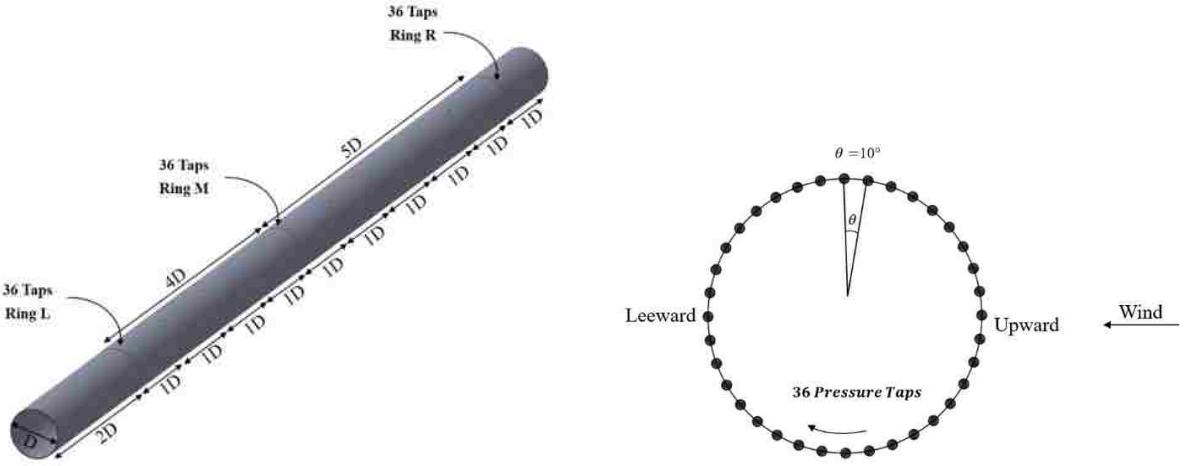


(a) Pressure taps on the cylinder model

(b) Distribution of pressure taps in a ring

Figure 2.3: Schematics illustrating the locations of surface pressure taps on the cylinder model.

## 2.4 Numerical Results and Verification with Measured Data

The objective of this paper is to demonstrate the capability of detached eddy simulations to predict aerodynamic loads on individual cables (of circular cross section) in static condition and in dynamic motion. Verification with existing experimental data in the literature, and data from new experiments conducted as a part of this study, are presented for static cylinders. Simulation capability is demonstrated for dynamic cases where harmonic solid body motions are considered. Smooth inflow is used – zero turbulence in the numerical simulations and the minimum possible inflow turbulence intensity (∼0.2%) in the tunnel. Cylinder surface is very smooth and hence surface roughness is not modeled in the simulations.

Static testing is performed for (1) flow normal to the cylinder axis, and (2) flow at an angle to the cylinder axis (inclined cylinder); three inclination angles are analyzed in this study. These cases are simulated at two Reynolds numbers – one corresponding to laminar separation (LS),

where transition to turbulence occurs in the shear layer, and one corresponding to turbulent separation (TS), where the boundary layer transitions before separation occurs, and it is the turbulent boundary layer that separates.

Dynamic testing is performed for cylinder oscillating with a prescribed frequency, with the flow normal to the cylinder axis. The oscillating cylinder is studied for two different oscillating directions: one is parallel to the flow direction and another one is perpendicular to the flow direction. Both dynamic cases are both simulated at same the Reynolds number $Re_D = 20,000$, and for the same oscillating frequency.

### 2.4.1 Mesh Sensitivity Study

A mesh sensitivity study is performed for the normally-incident flow case for both laminar and turbulent separation conditions. Table 2.1 presents a summary of the different cases simulated for this study. Three different meshes, labeled 'Mesh 1', 'Mesh 2', and 'Mesh 3' in the table are designed for laminar separation (LS). Corresponding to these are 'Mesh 4', 'Mesh 5', and 'Mesh 6' for turbulent separation (TS). The TS meshes are similar to LS meshes except the TS meshes have finer grids within the boundary layers in the radial direction to ensure $y^+ < 1$. The computational domain is $25\,D$ in the radial direction and $2\,D$ in the span direction.

Table 2.1: Summary of the test cases simulated to investigate sensitivity of results to mesh size

| **Separation type** | $\boldsymbol{Re_D}$ | **Mesh name** | **Cell count**$(\boldsymbol{\theta, r, z})$ |
|---|---|---|---|
| LS | 20,000 | Mesh 1 | 157, 233, 13 |
| LS | 20,000 | Mesh 2 | 236, 343, 20 |
| LS | 20,000 | Mesh 3 | 354, 507, 30 |
| TS | 140,000 | Mesh 4 | 157, 241, 13 |
| TS | 140,000 | Mesh 5 | 236, 350, 20 |
| TS | 140,000 | Mesh 6 | 354, 520, 30 |

Figure 2.4 compares the mean aerodynamic pressure coefficient, $\overline{C}_p = 2(\overline{p} - p_\infty)/(\rho V_\infty^2)$ obtained using simulations with different grids, and experimental data. Experiment I refers to

data from Norberg (2013) and Exp-ISU is from our measurements. The LS cases are simulated at cylinder diameter based Reynolds number, $Re_D = 20,000$, which is the same as Experiment I, but the $Re_D$ in Exp-ISU is higher ($Re_D = 51,500$) due to the limitation of the wind tunnel and measurement equipment. The data of Experiment II is from Roshko (1961) for the TS cases is at a much higher $Re_D$ of 8.4 M, but in the simulations, the $Re_D$ is increased until the boundary layer transitions to turbulence and then turbulent separation occurs; this occurs around $Re_D = 140,000$. The simulation results (time-mean quantities) become independent of $Re_D$ beyond this $Re_D$.

Consistent with the results of Travin et al. (2000) and Breuer (2000), the simulation results for LS are found to be sensitive to mesh size even with the highest mesh resolution attempted. Mesh 2 and Mesh 3 capture the flow separation location correctly (same as in the experiment), but separation is delayed with Mesh 1. Results of Mesh 2 are in closer agreement with Experiment I, however they differ from the results of Mesh 3 in the separated flow region. Interestingly, the Exp-ISU data agrees well with Mesh 3 results in the same region. For TS cases, the $\overline{C}_p$ distribution around the cylinder shows little sensitivity to mesh size variation; the distribution is more-or-less captured by all three meshes (Mesh 4, Mesh 5, & Mesh 6); the back pressure is very slightly over predicted.

Based on this study, Mesh 2 and Mesh 5 are chosen for the subsequent LS and TS simulations because they can predict aerodynamic loading and resolve wake turbulence reasonably accurately within a reasonable computational cost.

### 2.4.2 Static Cylinder with Normally-Incident Flow

The normally-incident, static-cylinder cases are further classified into two categories: (a) laminar separation (LS), and (b) turbulent separation (TS). Figure 2.5 plots iso-surfaces of the $Q$-criterion obtained from the simulations. The surfaces are colored by spanwise component of vorticity. Iso-surfaces of positive values of $Q$ show vortex structures, as $Q = 0.5\left(|\boldsymbol{\Omega}|^2 - |\boldsymbol{S}|^2\right) > 0$ in a vortex; $\boldsymbol{\Omega}$ and $\boldsymbol{S}$ are vorticity and rate-of-strain tensors respectively, and $|\boldsymbol{T}|$ denotes the Euclidean norm of the tensor $\boldsymbol{T}$.

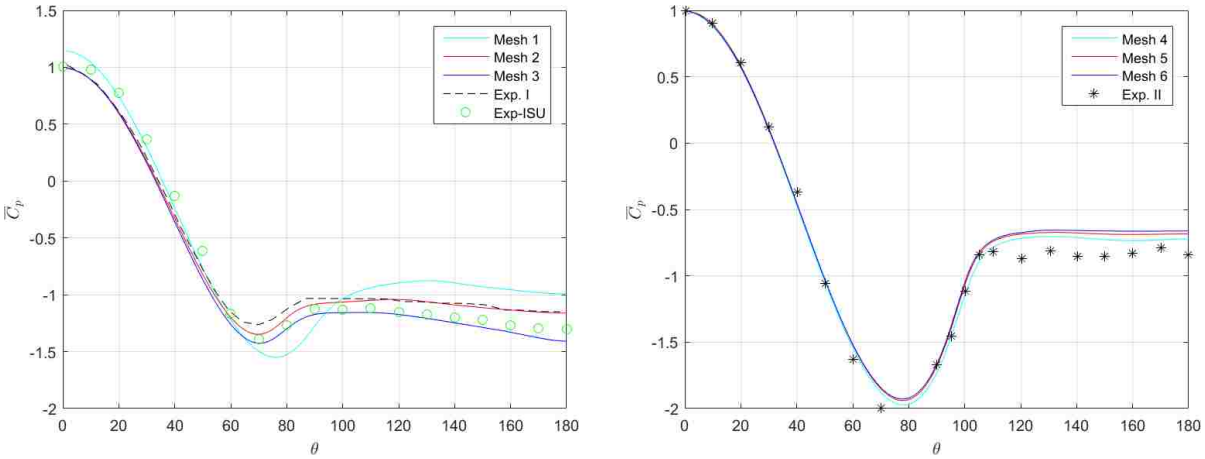


(a) $\overline{C}_p$ distribution, LS

(b) $\overline{C}_p$ distribution, TS

Figure 2.4: $\overline{C}_p$ comparisons between simulation results using different meshes for (a) laminar separation (LS), and (b) turbulent separation (TS). Simulations and experiments are both at $Re_D = 20,000$ for the LS. For TS, the $Re_D = 8.4$ M while the simulations are at $Re_D = 140,000$.

The organization of the vortices as alternately shed from either side of the cylinder (Karman vortex street) is clearly visible in Fig. 2.5. The vortices break down as they convect downstream; the mesh is resolved up to 8 cylinder diameters to capture the wake as it influences the unsteady loads on the cylinder. Figure 2.5 also shows that the laminar boundary layer separates much earlier in the case of LS as it cannot withstand adverse pressure gradient. In the TS case, the boundary layer naturally transitions to turbulent while attached to the surface; the turbulent boundary layer can better negotiate the adverse pressure gradient and hence the separation occurs further downstream. Another feature to note is the streamwise elongation of turbulent eddies in the TS case caused by the higher streamwise velocity; $Re_D$ is varied by varying the freestream velocity here.

#### 2.4.2.1 Laminar Separation, Normally-Incident Flow

Table 2.2 summarizes the simulation results for the laminar separation (LS) case and compares them with two sets of experimental data. The peak shedding Strouhal number ($St_p$), the mean drag coefficient, $\overline{C}_d$ and the mean back pressure coefficient, $\overline{C}_{pb}$ are compared in the table. Strouhal number is a non-dimensional frequency, defined here as $St = f\,D/V_\infty$, and $St_p$ corresponds to the frequency of wake shedding from the cylinder.

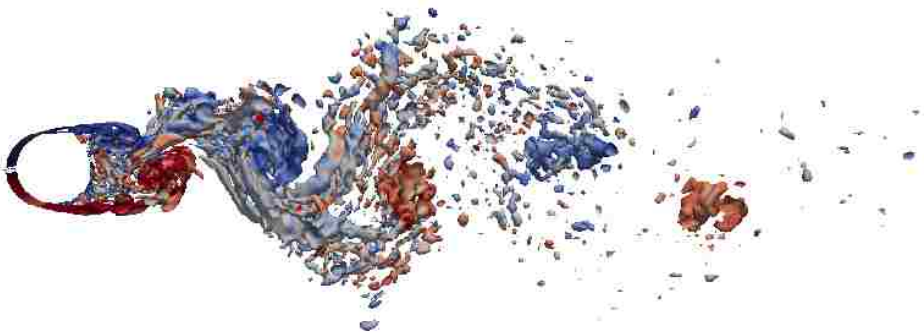

(a) Laminar separation, LS

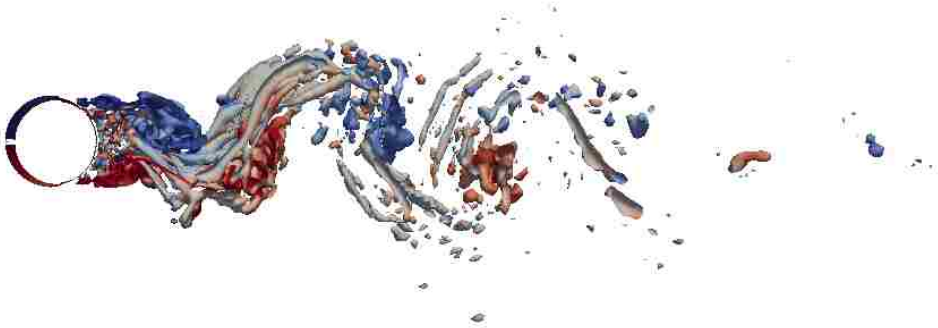

(b) Turbulent separation, TS

Figure 2.5: Iso-surfaces ($Q = 0.1$) of the $Q$ criterion with contours colored by component of vorticity vector in the span direction for (a) laminar separation (LS), simulation $Re_D = 20,000$, and (b) turbulent separation (TS), simulation $Re_D = 140,000$.

Figure 2.6 compares the predicted mean aerodynamic pressure coefficient, $\overline{C}_p$ and the root mean square of perturbation pressure coefficient, $C_{p'rms} = \left( \overline{C_p^2 - \overline{C}_p^2} \right)^{1/2}$ with the data from the two experiments. The predicted $\overline{C}_p$ agrees very well with the data from Experiment I; Exp-ISU data shows slightly lower $\overline{C}_p$ than observed in Experiment I and the simulation, especially after 100°, and the mean back pressure, $\overline{C}_{pb}$ is lower as well. The prediction $C_{p'rms}$ distribution lies in between the two measurements. Both measurements as well as the simulation show the peak to be around 80°, which indicates the location of flow separation for the LS case. The predicted distribution over the cylinder surface agrees well with the measurements.

Table 2.2: Summary of results for normally-incident flow simulations

| **Separation type** | $\boldsymbol{Re_D}$ | **Method** | $\boldsymbol{St_p}$ | $\boldsymbol{\overline{C}_d}$ | $\boldsymbol{\overline{C}_{pb}}$ |
|---|---|---|---|---|---|
| LS | 20,000 | $k-\omega$ DDES | 0.21 | 1.13 | -1.16 |
| LS | 20,000 | Experiment I | 0.19 | 1.22 | -1.1 |
| LS | 51,500 | Exp-ISU | 0.21 | 1.14 | -1.3 |

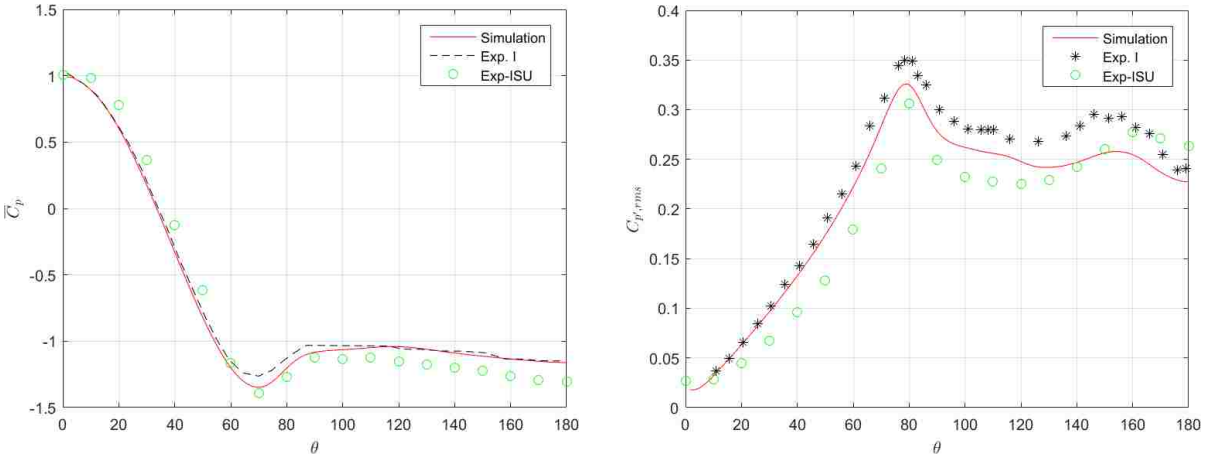


(a) Mean aerodynamic pressure coeff., $\overline{C}_p$

(b) r.m.s. of pressure coeff., $C_{p'rms}$

Figure 2.6: Comparisons of mean and rms of aerodynamic pressure coefficient between the simulation and experimental measurements for the laminar separation.

Figure 2.7 plots the predicted and measured wake velocity profiles at the axial station, $x/D = 2$; the cylinder axis is located at $x/D = 0$. The peak wake deficit and the wake profile are predicted accurately. The measured data shows a slight asymmetry in the data, which

is perhaps due to asymmetry in the experimental setup (e.g., distance from the tunnel wall between top and bottom of the cylinder). The simulation data is averaged over 120 wake shedding cycles and experimental data is averaged over 540 cycles.

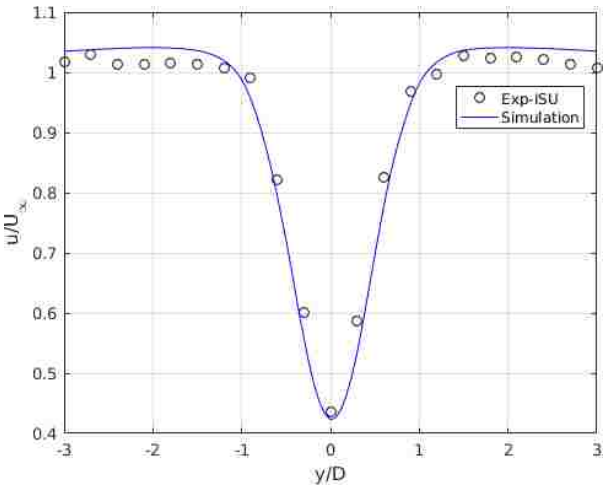


Figure 2.7: Comparison of predicted and measured velocity profiles in the cylinder wake $2D$ downstream of the cylinder axis.

Figure 2.8 presents predicted temporal variation of sectional lift and drag coefficients ($C_l$ and $C_d$). As expected for a circular cylinder, the mean lift coefficient ($\overline{C}_l$) is zero but the mean drag coefficient ($\overline{C}_d$) is finite. The high-frequency oscillations, more apparent in $C_l$ time history are due to Karman vortex shedding, which occurs at $St = fd/U \sim 0.2$ for bluff bodies in the range of $Re_D$ considered here. In addition to oscillations at the Karman vortex shedding frequency, the entire signal appears to modulate at a frequency which is an order of magnitude lower than that corresponding to $St = 0.2$. This modulation has a certain randomness to it and is not perfectly periodic. This modulation phenomenon has been reported elsewhere, see e.g., Travin et al. (2000).

Figure 2.9 (a) compares the power spectral densities of lift coefficient ($C_l$) between data from Exp-ISU and the simulation for the LS case. The lift in the measurements is obtained by integrating the surface pressure measured using pressure taps. Figure 2.9 (b) presents the DES computed spectra of $C_d$. Because vortex shedding alternates between the top and bottom sides of the cylinder (see Fig. 2.5), one vortex shedding period contains two cycles of drag but only one cycle of lift. This can be seen in Figure 2.9, where the spectral peak for $C_l$ occurs at $f$ while

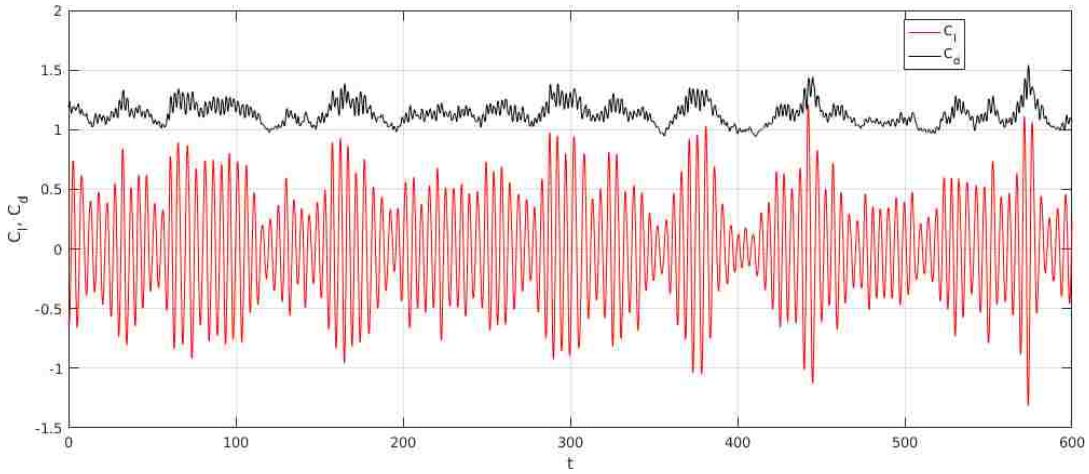


Figure 2.8: Predicted temporal variations of lift and drag coefficients for the laminar separation (LS) case

the spectral peak for drag is at $2 \times f$, where $f$ is determined by the peak shedding Strouhal number, $St_p = f\,D/V_\infty$. Based on existing literature (see Travin et al. (2000) and Norberg (2013)), $St_p \sim 0.2$. Both measurement and prediction agree very well with each other and show the peak for lift to be around $f$ corresponding to $St_p$.

The peak frequency and its first three harmonics that occur at $St = 0.4, 0.6, \& 0.8$, are identified in the figure using vertical grid lines and labeled as $2f$, $3f$, $\& 4f$. The prediction and experiment both show a second, smaller peak in the lift spectrum at the third harmonic ($St = 0.6$). Since the lift vector alternates with the side the vortex sheds from, only odd harmonics of $f$ (i.e., $3f$, $5f, \ldots$) are expected in the spectra. Therefore, no peak is observed in the lift spectra at the second harmonic ($St = 0.4$) or higher *even* harmonics in either the measured or the simulated data. The spectral shape of PSD of $C_l$ is correctly predicted, even though the magnitude is slightly higher than the measured data.

#### 2.4.2.2 Turbulent Separation, Normally-Incident Flow

Table 2.3 summarizes the simulation results for the turbulent separation (TS) case and compares them with the experimental measurements from Roshko (1961). It is re-emphasized that the experimental data for the TS case is at a much higher Reynolds number, $Re_D = 8.4$M compared to the simulations, which are carried out at $Re_D = 140,000$. However, the results

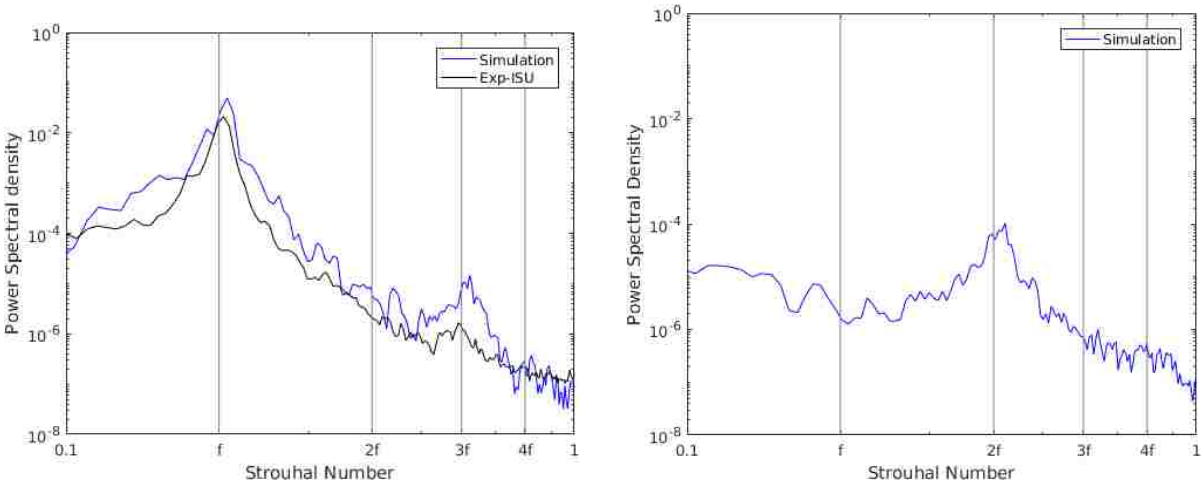


(a) PSD of $C_l$ (b) PSD of $C_d$

Figure 2.9: Comparison of predicted and measured power spectral densities (PSDs) of $C_l$ and $C_d$ for the laminar separation (LS) case. The measured data here is from our experiments (Exp-ISU).

have weak dependence on $Re_D$ for the TS cases. The predicted peak shedding Strouhal number, $St_p$ and the mean aerodynamic pressure coefficient, $\overline{C}_p$ (see Fig. 2.4 (b)), agree well with the measured data. However, the mean back pressure $\overline{C}_{pb}$ is over-predicted in the simulation, which causes $\overline{C}_d$ to be under-predicted.

Figure 2.10 plots the predicted time histories of $C_l$ and $C_d$ for the TS case. Periodic oscillations corresponding to the vortex shedding frequency are observed. As in the laminar separation (LS) case, the temporal variation of $C_l$ for the TS case also displays modulation of the signal with a frequency much lower than the vortex shedding frequency. Predicted power spectral densities (PSDs) of $C_l$ and $C_d$ for the TS case are plotted in Fig. 2.11. The results show that $St_p = 0.29$, which is slightly higher than the $St_p$ for the LS case ($\sim 0.2$). The Peak PSD is also significantly lower for the TS case compared to the LS case.

Comparing the iso-surface plots in Fig. 2.5 between the LS and TS cases shows a delayed separation and consequently a narrower wake for the TS case. Due to separation delay, the form drag is reduced and hence the mean drag coefficient ($\overline{C}_d$) in the TS case is lower than in the LS case (see Table 2.3). The delayed separation and narrower wake are also the reasons behind significantly reduced unsteady lift PSD for the TS case.

Table 2.3: Summary of results for normally-incident flow simulations

| **Separation type** | $Re_D$ | **Method** | $St_p$ | $\overline{C}_d$ | $\overline{C}_{pb}$ |
|---|---|---|---|---|---|
| TS | 140,000 | $k-\omega$ DDES | 0.29 | 0.58 | -0.7 |
| TS | 8,400,000 | Experiment II | 0.28 | 0.7 | -0.8 |

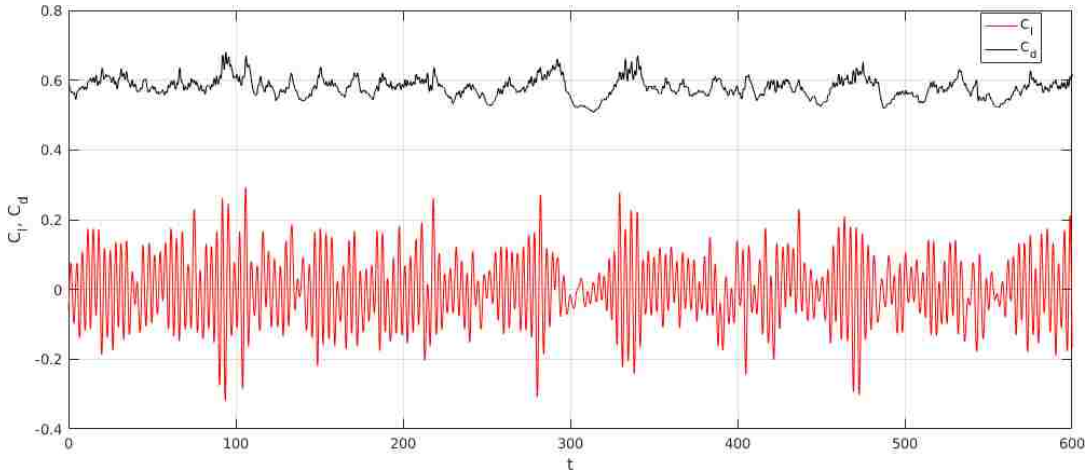


Figure 2.10: Predicted temporal variations of lift and drag coefficients for the turbulent separation (TS) case.

### 2.4.3 Static Cylinder with Yawed Flow (Inclined Cylinder)

Figure 2.12 is a schematic that illustrates the setup for the inclined-cylinder simulations. The relative inclination of the cylinder axis with respect to the flow is obtained by yawing the flow rather than inclining the cylinder; these simulations are therefore also referred to as yawed flow simulations. Other than yawing the inflow, the setup is exactly the same as for the normally-incident flow cases.

The yaw angle, $\beta$ is defined as the angle between the inflow velocity vector $\boldsymbol{V_\infty}$ and the $x$ axis; the cylinder is aligned with the $z$ axis. The normal component of the flow velocity, $V_n$ and the spanwise component, $V_z$ are defined as $V_n = V_\infty \cos\beta$ and $V_z = V_\infty \sin\beta$, where $V_\infty = |\boldsymbol{V_\infty}|$. The computational domain is extended to $10 \times D$ in the spanwise direction for yawed flow cases to resolve and investigate spanwise variation of aerodynamic forces. Three different yaw angles $\beta = 15$, 30, & 45 degrees are investigated for both LS and TS.

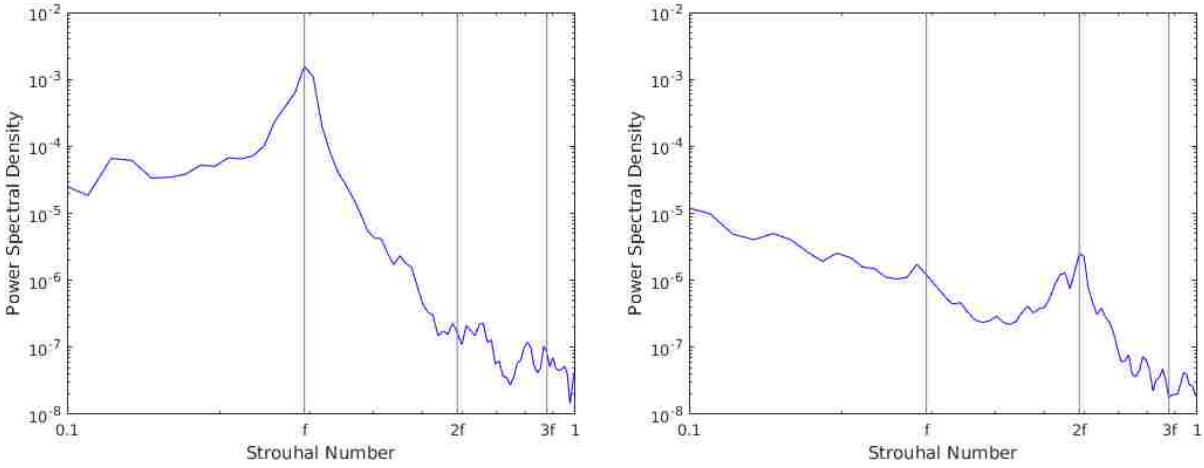


(a) PSD of $C_l$ (b) PSD of $C_d$

Figure 2.11: Predicted power spectral densities of $C_l$ and $C_d$ for the turbulent separation (TS) case.

#### 2.4.3.1 Laminar Separation, Yawed Flow

Table 2.4 summarizes the peak Strouhal number ($St_p$) and the back pressure coefficient ($C_{pb}$) for four different flow yaw angles, $\beta = 0, 15, 30, \& 45$ degrees for laminar separation (LS). The span dimension for the zero-degree case is increased to $10 \times D$ for this comparison, to be consistent with others yawed flow simulations. The component of the freestream velocity normal to the cylinder axis is used as the reference velocity scale to define a new set of non-dimensional quantities, such as Reynolds number, $Re_{D,n} = \rho V_n D/\mu$, Strouhal number $St_{p,n} = f\,D/V_n$, and aerodynamic pressure coefficient $\overline{C}_{p,n} = 2(\overline{p} - p_\infty)/(\rho V_n^2)$. The peak shedding Strouhal number and the mean back pressure coefficient normalized in this manner are labeled respectively as $St_{p,n}$ and $\overline{C}_{pb,n}$. The measured value of $\overline{C}_{pb,n}$ is lower than predicted by the simulations (see Table 2.4), suggesting that the mean velocity at the back of the cylinder is slightly higher than predicted by the simulations.

Figure 2.13 compares with measured data the predicted mean aerodynamic pressure coefficient ($\overline{C}_{p,n}$) and root mean square of perturbation pressure coefficient, $C_{p'rms,n}$ normalized using $V_n$, for $\beta = 30°$ case. The predicted distribution of $\overline{C}_{p,n}$ and mean back pressure, $\overline{C}_{pb,n}$ are found to be slightly higher than Exp-ISU data, which is consisted with the observation for the normally-incident flow cases. The predicted $C_{p'rms,n}$ distribution agrees very well with

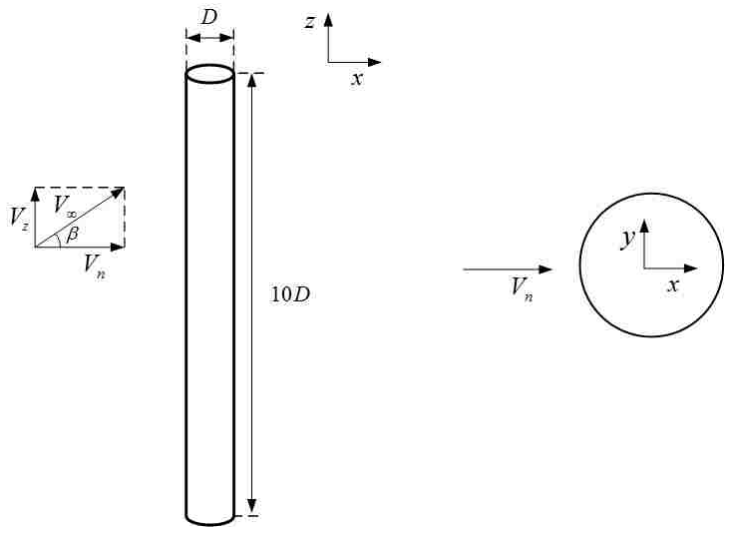


Figure 2.12: A schematic of the computational setup for static inclined cylinder simulations. The right figure is a cross-sectional view of the cylinder. The inflow is set to an angle with respect to the cylinder axis, which stays aligned with the $z$ axis of the coordinate system.

Table 2.4: Summary of simulation results for four different flow yaw angles ($\beta = 0, 15, 30,$ & 45 deg). Experimental data is only shown for $\beta = 30°$.

| **Method** | **flow angle, $\beta$** | $\boldsymbol{Re_D}$ | $\boldsymbol{Re_{D,n}}$ | $\boldsymbol{St_{p,n}}$ | $\boldsymbol{\overline{C}_{pb,n}}$ |
|---|---|---|---|---|---|
| Simulation | 0° | 20,000 | 20,000 | 0.21 | -1.15 |
| Simulation | 15° | 20,000 | 19,318 | 0.21 | -1.11 |
| Simulation | 30° | 20,000 | 17,320 | 0.20 | -1.11 |
| Exp-ISU | 30° | 51,500 | 44,600 | 0.19 | -1.27 |
| Simulation | 45° | 20,000 | 14,142 | 0.21 | -1.16 |

measurement, especially before 120°. The peak of $C_{p'rms,n}$ is observed around 80° in both experiment and simulation, which is indicative of the location of separation of the shear layer. Beyond $\theta = 120°$, the measured data shows higher $C_{p'rms,n}$ than predicted by the simulations. A similar underprediction is observed in the normally-incident flow case.

Figure 2.14 presents predicted and measured wake velocity profiles for $\beta = 30°$ case at $x/D = 2$. The predicted peak wake deficit matches remarkably well with Exp-ISU data. However, the experimental data shows higher overshoots in streamwise velocity in the shear layer region than predicted by the simulations. The experimental data is also very slightly

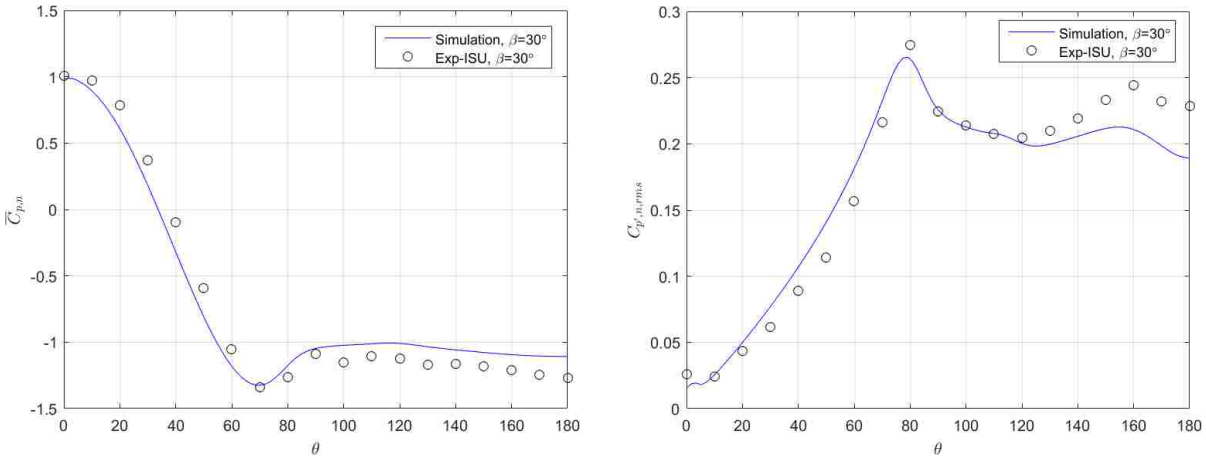


(a) Mean pressure distribution, $\overline{C}_{p,n}$ (b) rms of perturbation pressure, $C_{p'rms,n}$

Figure 2.13: Comparisons between simulation and experimental measurements for $\beta = 30°$ yawed-flow case.

asymmetric, which is likely due to the fact that one side of the cylinder is closer to the tunnel wall. It should be noted that the asymmetry is very small and thus the wall effects are minimal.

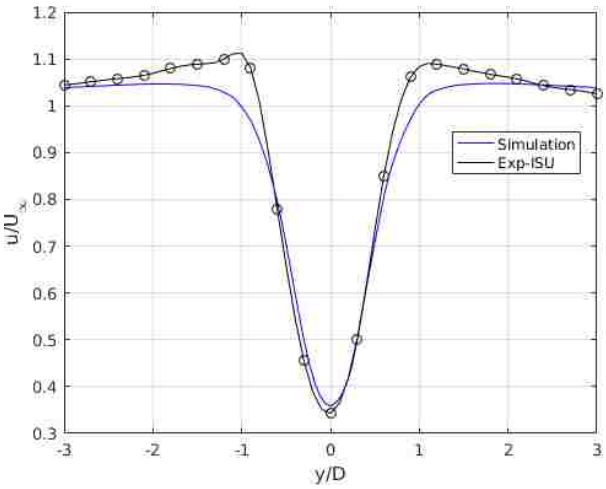


Figure 2.14: Comparison of predicted and measured velocity profiles for $\beta = 30°$ yawed flow in the cylinder wake $2D$ downstream of the cylinder axis

Figure 2.15 compares the power spectral densities of the transverse force coefficient (along the $y$ axis), $C_{y,n}$ for $\beta = 30°$ case between Exp-ISU data and predictions, where $C_{y,n} = 2\,F_y/\left(\rho V_n^2 (D \times L)\right)$, $F_y$ is the net force over the entire cylinder; longitudinal force coefficient,

$C_{x,n}$ is defined similarly. In the simulation, the first peak is observed around $St_{p,n} \sim 0.2$, which is the same as for the normally-incidence flow case (see Figure 2.9 (a)). The spectral shape is correctly predicted by the simulation although the measured curve appears to be shifted along the $x$ axis; this is likely due to a scaling factor in frequency (log scale is used for frequency in Fig. 2.15) coming from slight mismatch in measurement of inflow velocity in the experiment. Figure 2.16 compares the predicted mean aerodynamic pressure coefficient ($\overline{C}_{p,n}$) normalized

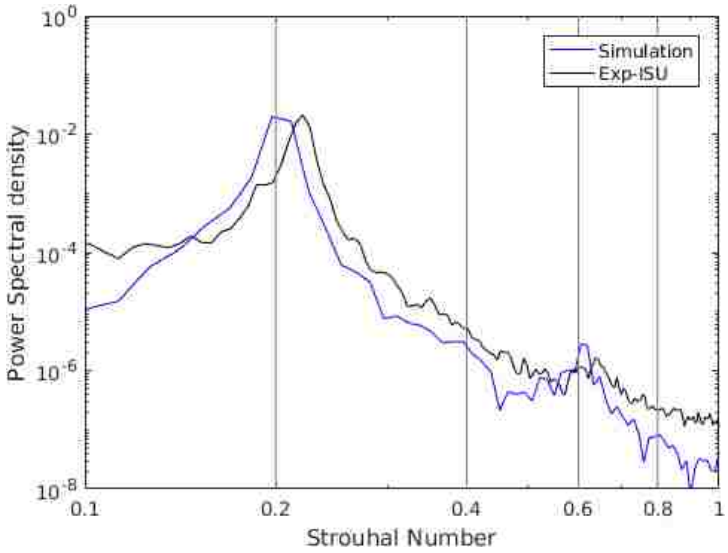


Figure 2.15: Comparison of predicted and experimental power spectral densities (PSDs) of force coefficient $C_{y,n}$ for $\beta = 30°$ yawed-flow cases.

using $V_n$, for four different values of inflow yaw angle, $\beta$. The distribution of $\overline{C}_{p,n}$ is found to be very similar irrespective of $\beta$; Zdravkovich (2003) refers to this as 'independence principle'. The independence principle is also observed in the power spectral densities of the transverse force coefficient, $C_{y,n}$ for the different values of $\beta$ analyzed. Figure 2.16 (b) shows that the spectra collapse when $V_n$ is used to normalize the coefficients and the frequency; the abscissa in Fig. 2.16 (b) is $St_n$.

Figure 2.17 shows spatio-temporal plots of the the force coefficients $C_{x,n}$ and $C_{y,n}$. Here, $C_{x,n}$ and $C_{y,n}$ are functions of spanwise location and are computed by normalizing the sectional forces in $x$ and $y$ directions respectively ($C_{x,n} = 2\,f_x/(\rho V_n^2)$, where $f_x$ is force per unit area in the $x$ direction). The coefficients are plotted as functions of span ($z$) and time to obtain the contours shown in the figure. The contours clearly show that the force coefficients vary along

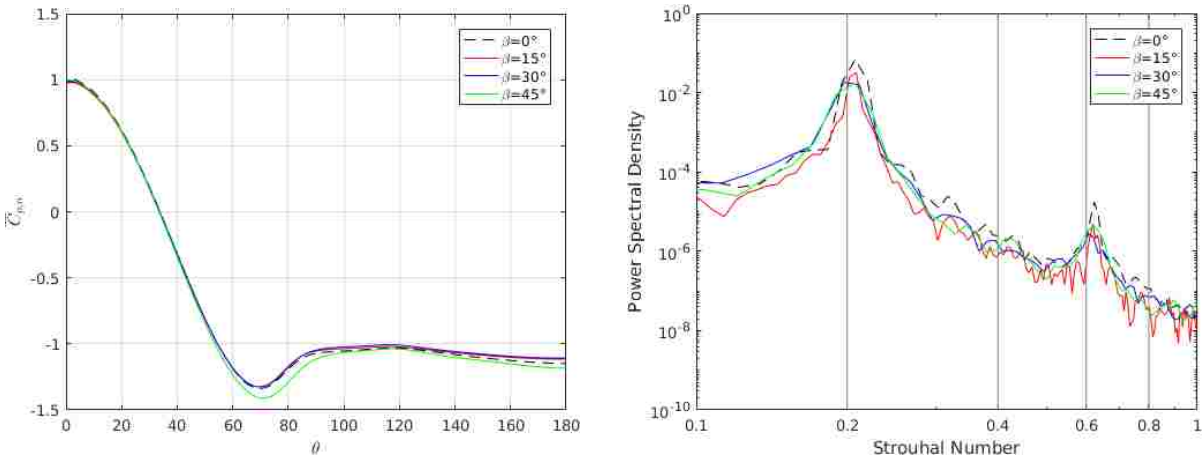


(a) Mean pressure coeff., $\overline{C}_{p,n}$ (b) PSDs of $C_{y,n}$

Figure 2.16: Independence principle: comparisons between predictions for the laminar separation (LS) case for various $\beta$ values of (a) $\overline{C}_{p,n}$, and (b) power spectral densities (PSDs) of $C_{y,n}$.

the span, indicating that vortex shedding does not occur simultaneously along the entire span. In fact, a spatial drift from left to right with increasing time can be seen in the contours (more visible in the $C_{x,n}$ spatio-temporal plot) which is indicative of spanwise flow over the cylinder.

Figure 2.18 presents coherence of force coefficients for $\beta = 30°$ case. Magnitude squared coherence, $\gamma^2(\Delta z)$ is defined as

$$\gamma^2(\Delta z) = \frac{\langle |S_{xy}|^2 \rangle}{\langle S_{xx} \rangle \langle S_{yy} \rangle}, \tag{2.1}$$

where $S_{xy}$ denotes cross-spectral density of the quantity ($C_{x,n}$ or $C_{y,n}$) at two points separated by a distance $\Delta z$, and $S_{xx}$, $S_{yy}$ are auto-spectral densities; angular brackets denote ensemble averaging, however ergodicity assumption is used to relate that to time averaging. The coherence plot of $C_{y,n}$ indicates that spanwise correlation is very high (over nearly the entire cylinder span) at the vortex shedding frequency, but is small at other frequencies, which is expected based on literature. Drag force coefficient however is not that highly correlated along the span even at the peak vortex shedding frequency.

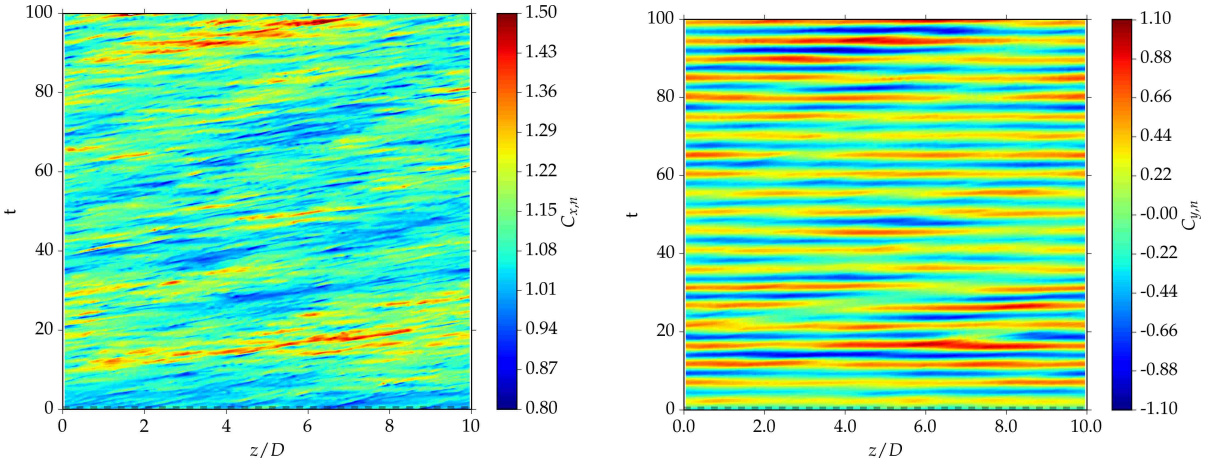


(a) $C_{x,n}$ (b) $C_{y,n}$

Figure 2.17: Spatio-temporal distribution of force coefficients at $\beta = 30°$ for laminar separation (LS)

#### 2.4.3.2 Turbulent Separation, Yawed Flow

Table 2.5 summarizes the numerical results of the normally-incident flow and yawed flows for turbulent separation (TS). The normally-incident flow ($\beta = 0°$) and the $\beta = 15°$ case have a much higher peak shedding Strouhal number, $St_{p,n}$ than observed for the other two yawed flow cases ($\beta = 30°$ and $45°$). A similar "grouping" is observed in Fig. 2.19 in the distribution of $\overline{C}_{p,n}$ over the cylinder surface. While the $\overline{C}_{p,n}$ distributions for $\beta = 0°$ and $15°$ are clustered together and look similar, the distributions for $\beta = 30°$ and $45°$ are substantially different. This is primarily because the Reynolds number of importance here is that based on the normal component of flow velocity, i.e., $Re_{D,n}$ and not that based on velocity magnitude, $Re_D$. Table 2.5 lists these two Reynolds numbers for each case. As the yaw angle increases, $V_n$ drops and along with it $Re_{D,n}$ drops as well. As $Re_{D,n}$ drops, the boundary layer does not transition completely to turbulent, and hence the separation type does not stay turbulent for all flow angles.

Figure 2.20 shows spatio-temporal plots for $C_{x,n}$ and $C_{y,n}$ for $\beta = 30°$ with turbulent separation (TS). Spanwise flow is clearly visible in the $C_{x,n}$ plot with the drift in $C_{x,n}$ contours from left to right with increasing time. This drift is more perceptible for TS than it is for LS (compare Fig 2.20 (a) with Fig. 2.17 (a)).

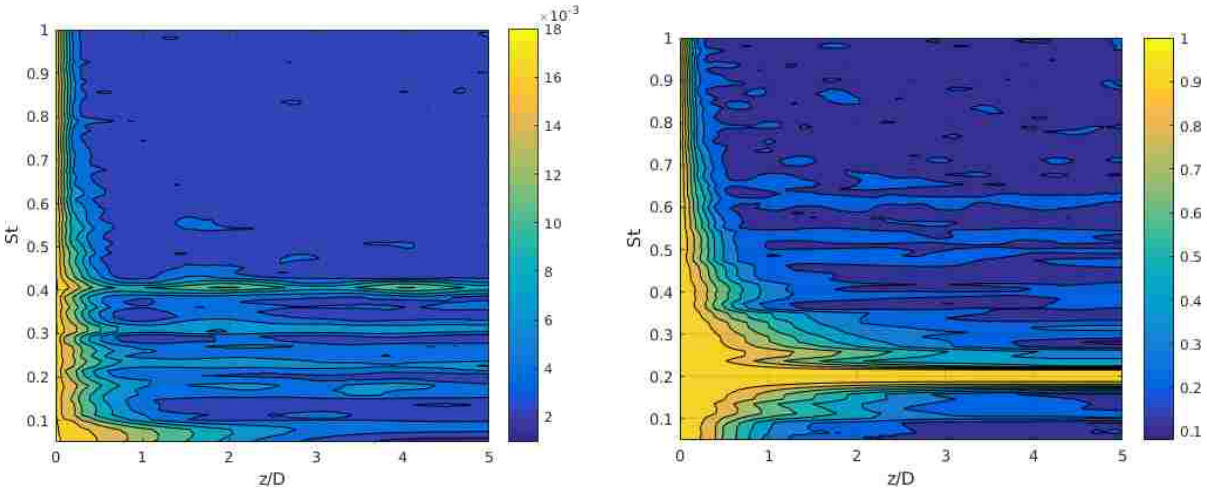


(a) $C_{x,n}$ (b) $C_{y,n}$

Figure 2.18: Magnitude squared coherence, $\gamma^2(\Delta z)$ of transverse and longitudinal force coefficients, $C_{x,n}$ and $C_{y,n}$ for $\beta = 30°$ case.

Table 2.5: Summary of simulation and experimental results of normally-incident flow ($\beta = 0$) and yawed flow simulations for turbulent separation (TS)

| **Method** | **flow angle, $\beta$** | $\boldsymbol{Re_D}$ | $\boldsymbol{Re_{D,n}}$ | $\boldsymbol{St_{p,n}}$ | $\boldsymbol{\overline{C}_{pb,n}}$ |
|---|---|---|---|---|---|
| Simulation | 0° | 140,000 | 140,000 | 0.29 | -0.65 |
| Simulation | 15° | 140,000 | 135,223 | 0.29 | -0.65 |
| Simulation | 30° | 140,000 | 121,244 | 0.24 | -0.65 |
| Simulation | 45° | 140,000 | 98,995 | 0.24 | -0.71 |

### 2.4.4 Dynamic Cases

Galloping is an inherently unsteady phenomenon where a cable experiences high-amplitude oscillations. Aerodynamic loads on the cable need to be estimated in such dynamic state for an aeroelastic load model to predict galloping. In the previous sections we verified the ability of the solution methodology to predict aerodynamic loads when the cable is static, for different cable inclination angles angles. In order to better understanding the aerodynamics of high-amplitude galloping cables, investigations of a harmonically oscillating (prescribed motion) cylinder are performed and presented in this section. In order to handle cylinder motion, the dynamic mesh method available in OpenFOAM is used. This method specifies the motion of

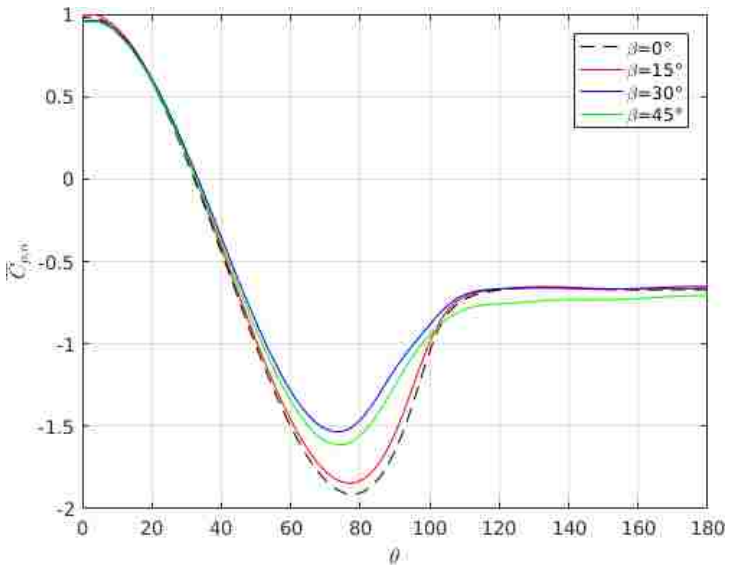


Figure 2.19: Comparison of $\overline{C}_{p,n}$ between normally-incident flow and different yawed flows for the turbulent separation (TS) cases

boundaries according to the prescribed motion and then uses the solution to determine the new point positions from the old ones. Since we prescribe the motion of outer boundary of the computational domain, the whole computational domain/mesh is moved according to the prescribed motion.

We consider a harmonically oscillating cylinder in normally-incident flow. Two cylinder oscillation directions are considered: streamwise (along the flow, $x$ direction), and transverse (normal to the flow, along the $y$ direction). The prescribed frequency of oscillation is 1/100 of the vortex shedding frequency, and the peak vibration amplitude is $0.5 \times D$. Figure 2.21 presents a schematic of the setup for the dynamic cylinder simulations.

Figure 2.22 plots the $\overline{C}_p$ and $C_{p'rms}$ results for streamwise and transverse cylinder vibration cases respectively. Also shown in the figure with dashed lines are results for the corresponding static case. For streamwise vibration, the $\overline{C}_p$ is only slightly lower than for the static case. $C_{p'rms}$ however, more than triples due to the motion of the cylinder. It should be borne in mind that $C_{p'rms}$ in dynamic cases gets contributions from the deterministic prescribed motion of the cylinder, in addition to that due to the stochastic turbulent field. The increase is particularly large at the leading stagnation point ($\theta = 0°$) where there is virtually no unsteady pressure in

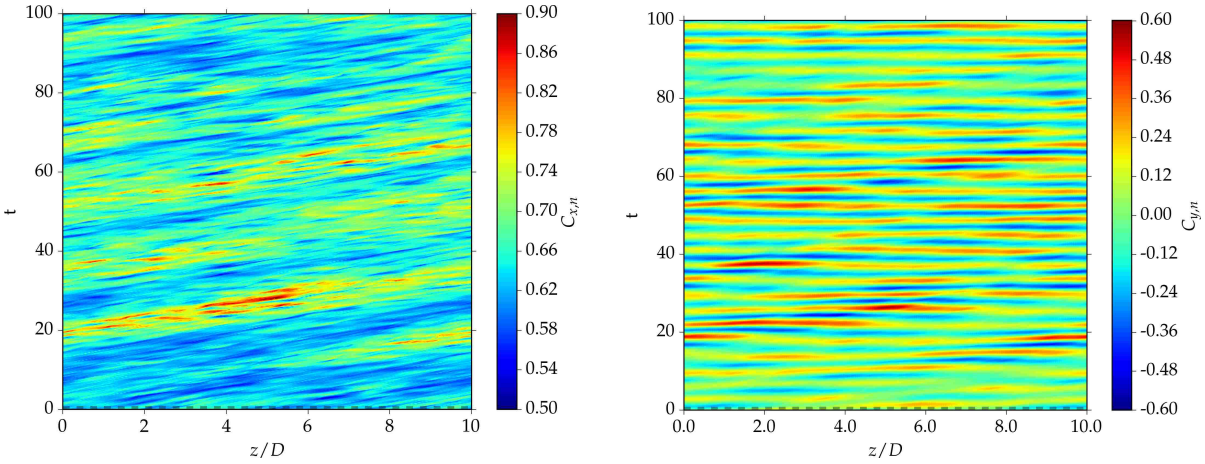


(a) $C_{x,n}$ (b) $C_{y,n}$

Figure 2.20: Spatial-temporal distribution of force coefficients at $\beta = 30°$ for turbulent separation (TS)

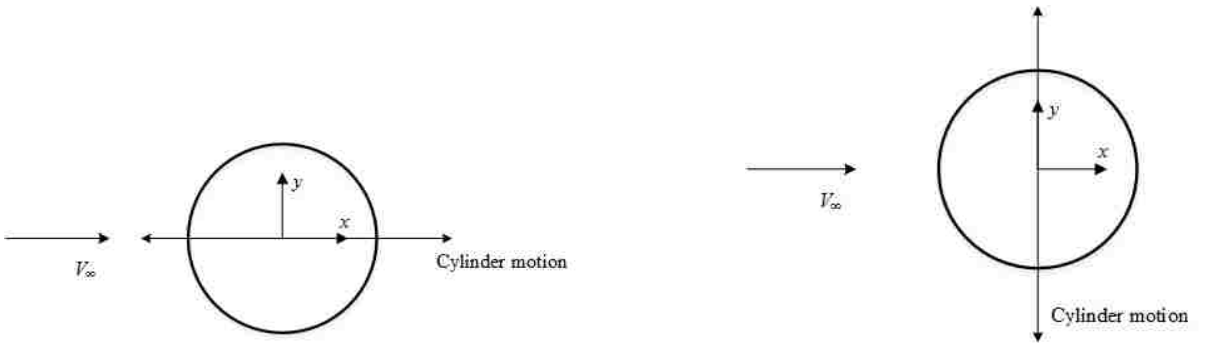


(a) Streamwise vibration, along the $x$ axis (b) Transverse vibration, along the $y$ axis

Figure 2.21: A schematic of the computational setup for dynamic cases.

the static condition. The first peak of $C_{p'rms}$ is around 80°, as in the static case, indicating that the boundary layer separation location does not change due to the cylinder motion.

Figure 2.23 plots the corresponding results for the transverse vibration case. For the selected values of amplitude and frequency of vibration, the results of transverse vibration are dramatically different from those for streamwise vibration. The increases in $\overline{C}_p$ and $C_{p'rms}$ are much more substantial than for the streamwise vibration case, except near the leading the trailing stagnation regions ($\theta = 0°$ and 180°). A cylinder moving in the transverse direction behaves as a lifting body in an unsteady sense, with the motion giving the cylinder an effective

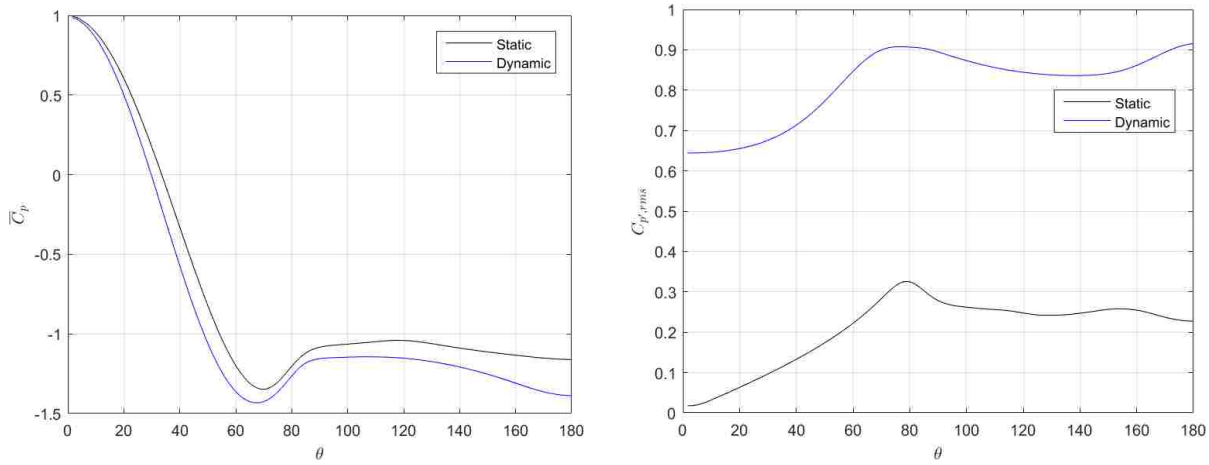


(a) Mean pressure distribution, $\overline{C}_p$ (b) rms of perturbation pressure, $C_{p'rms}$

Figure 2.22: $\overline{C}_p$ and $C_{p'rms}$ for a streamwise oscillating cylinder at $Re_D = 20,000$

camber. Increase in $\overline{C}_p$ and $C_{p'rms}$ due to transverse vibration are therefore much higher than for streamwise vibration. Also, the peak of $C_{p'rms}$ for transverse vibration is around 85°, which indicates that the boundary layer separation is delayed due to vibration.

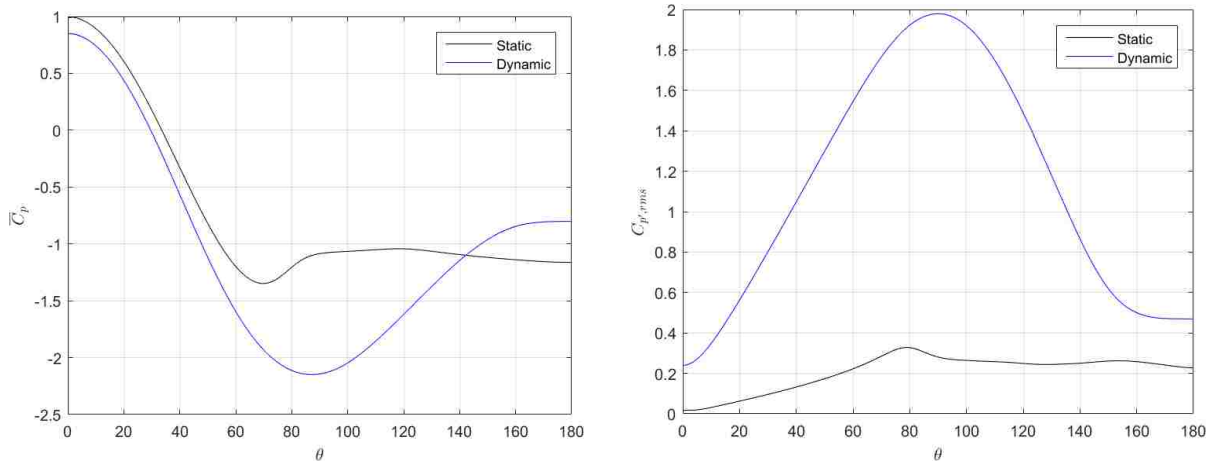


(a) Mean pressure distribution, $\overline{C}_p$ (b) rms of perturbation pressure, $C_{p'rms}$

Figure 2.23: $\overline{C}_p$ and $C_{p'rms}$ for a transverse oscillating cylinder at $Re_D = 20,000$

Figure 2.24 plots temporal variations of lift and drag coefficients for the two dynamic simulations. As expected, amplitudes of force $C_l$ of both dynamic cases are much higher than for corresponding the static cases (see Fig. 2.8). The amplitude of $C_l$ oscillations for the transverse vibration case are nearly twice of that observed for the streamwise vibration case,

corroborating the results of $C_{p'rms}$ in Fig. 2.23. The unsteady drag increase however, is larger for the streamwise oscillation case. Essentially, the component of unsteady force that increases more is consistent with the direction of vibration – for streamwise vibration it is the force in the $x$ direction (drag) and for transverse vibration, it is the force in the $y$ direction (lift). This can be justified by the contribution of the "apparent mass" in unsteady lift as described by Karman and Sears (1938).

Figure 2.25 shows PSDs of $C_l$ for the two dynamic simulations. In Figure 2.25 (a), The first peak in the spectrum corresponds to the peak vortex shedding and is at $St \sim 0.16$, which is close to $St \sim 0.2$ found for the corresponding static case. In Fig. 2.25 (b), the first peak is around $St \sim 0.018$, which corresponds to the frequency of the prescribed harmonic motion. The frequency of the prescribed harmonic oscillations however, is not observed in the spectrum for the streamwise vibration case because the oscillation of the cylinder simply modulates the $C_l$ oscillations caused by vortex shedding.

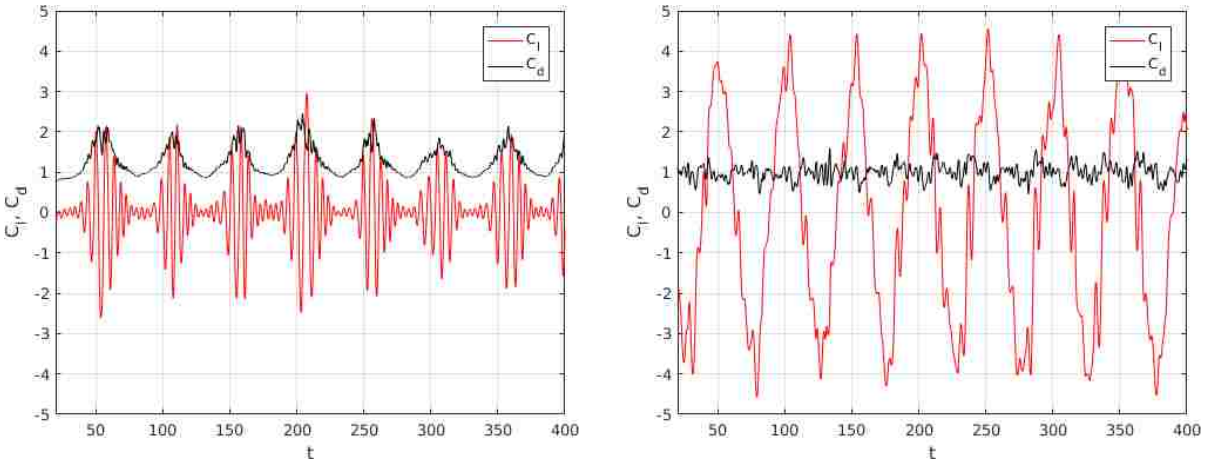


(a) Streamwise vibration

(b) Transverse vibration

Figure 2.24: Predicted temporal variations of lift and drag coefficients for dynamic cases at $Re_D = 20,000$

This demonstrates the capability of the solver to predict unsteady loads on cylinders in dynamic motion, which is required to develop a load model for predicting dry cable vibration.

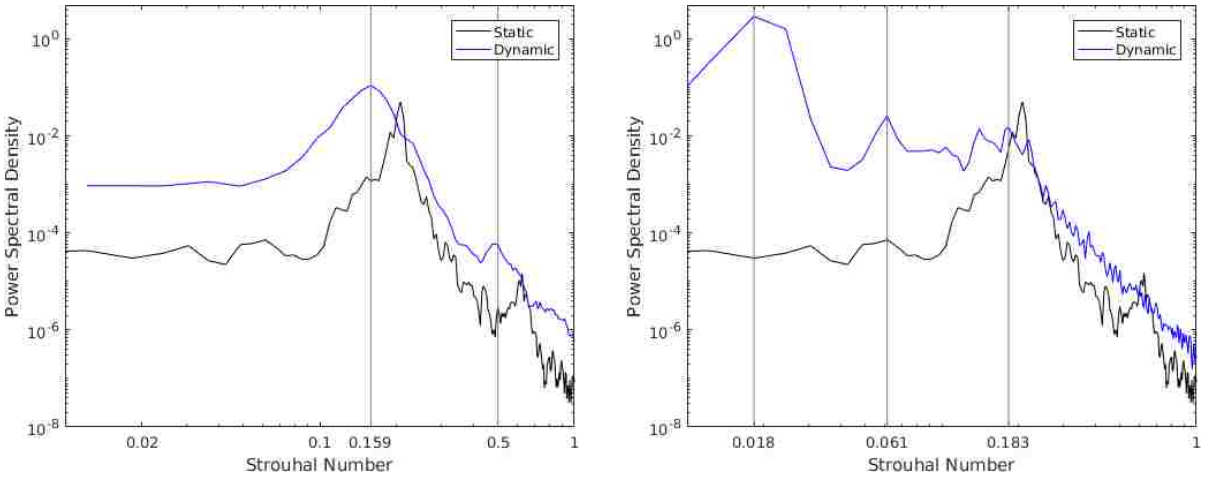


(a) Streamwise vibration

(b) Transverse vibration

Figure 2.25: Comparison of predicted power spectral densities (PSDs) of $C_l$ for dynamic cases at $Re = 20,000$

## 2.5 Conclusion

A computational methodology based on a $k-\omega$ delayed detached eddy simulation (DDES) model and in-house experiments are used to investigate aerodynamic loading on a smooth circular cylinder. Simulations are performed for the cylinder in normally-incident flow (static and dynamic) and yawed flow (3 cases) under two conditions – (1) when the cylinder boundary layer separates while it is laminar (LS), and (2) when the boundary layer transitions to turbulence before separation (TS). The computational methodology for predicting aerodynamic loading on the cylinder is verified against experimental data in normally-incident flow and $\beta = 30°$ yawed flow. The agreement between simulations and experiments with normally-incident flow in both LS and TS is very good, and the result of the yawed flow simulation with $\beta = 30°$ is reasonable in comparison with experiment. Overall, these comparisons show that the computational methodology is able to accurately predict aerodynamic loading on a static, smooth circular cylinder in smooth inflow.

Comparisons of simulation results for different yawed flows show that the aerodynamic loads do not vary with yaw angle ($\beta$) when the aerodynamic loads and vortex shedding frequency are non-dimensionalized using the component of the flow velocity normal to the cylinder axis.

This indifference to yaw angle, referred to as independence principle, is observed in the LS simulation results.

The capability of the solver to perform dynamic simulations with prescribed motion is demonstrated for a smooth cylinder in normally-incident flow. Harmonically oscillating cylinder simulations are performed for two cases: cylinder oscillating in the streamwise direction and in the transverse direction. Aerodynamic loading is found to vary significantly due to cylinder motion, proving that dynamic simulations are essential to obtain accurate unsteady loading, which is required by aeroelastic load models to predict dry cable vibration.

## 2.6 Acknowledgments

Funding for this research is provided by the National Science Foundation (Grant #NSF/ CMMI-1537917). Computational resources are provided by NSF XSEDE (Grant #TG-CTS130004).

# CHAPTER 3. CONCLUSION

A computational methodology based on a $k-\omega$ delayed detached eddy simulation (DDES) model is used to investigate aerodynamic loading on a smooth circular cylinder. Simulations are performed for the cylinder in normally-incident flow (static and dynamic) and yawed flow (3 cases) under two conditions – (1) when the cylinder boundary layer separates while it is laminar (LS), and (2) when the boundary layer transitions to turbulence before separation (TS). The computational methodology for predicting aerodynamic loading on the cylinder is verified against experimental data in normally-incident flow and $\beta = 30^\circ$ yawed flow. The agreement between simulations and experiments with normally-incident flow in both LS and TS conditions is very good, and the result of yawed flow simulation with $\beta = 30^\circ$ is reasonable in comparison with experiment. Overall, these comparisons show that the computational methodology is able to accurately predict aerodynamic loading on a static, smooth circular cylinder in smooth inflow.

Comparisons of simulation results for different yawed flows show that the aerodynamic loads do not vary with yaw angle $\beta$ when the loads and frequency are non-dimensionalized using the component of the flow velocity normal to the cylinder axis. This indifference to yaw angle, referred to as independence principle, is observed in the LS simulation results.

The capability of the solver to perform dynamic simulations with prescribed motion is demonstrated for a smooth cylinder in normally-incident flow. Harmonically oscillating cylinder simulations are performed for two cases: cylinder oscillating in the streamwise direction and in the transverse direction. Aerodynamic loading is found to vary significantly due to cylinder motion, proving that dynamic simulations are essential to obtain accurate unsteady loading, which is required by aeroelastic load models to predict dry cable vibration.

## 3.1 Prospects for Future Work

This thesis has demonstrated the capability of the proposed computational methodology based on a $k-\omega$ DDES model to investigate aerodynamic loading on a smooth circular cylinder in static and dynamic conditions. However, in order to better understand the aeromechanics of galloping and actually predict galloping, the following should be pursued:

- Harmonically oscillating cylinder simulations in this thesis are only performed for two canonical, prescribed cylinder motions in normally-incident flow. In order to reproduce dry-cable galloping for inclined cylinders in the simulation, more harmonically oscillating cylinder simulations with different yawed flow ($\beta \neq 0$) and different prescribed motions are required. Further measurements of dry-cable galloping are also required to validate the results of the simulations.

- A new simulation can be performed in spatially and temporally varying span-wise nonuniform flow (like in atmospheric boundary layer wind) and transient flow or gust (like in non-synoptic wind) in order to study the effects of nonuniform flow. Another simulation with wake-induced flow can be performed with a static cylinder in proximity of an oscillating cylinder. This will improve our understanding of wake galloping.

- Finally, an aeroelastic load model should be developed that uses the computational results to derive the appropriate flutter derivatives and/or rational functions. This load model can be used to predict aeroelastic behavior of a cable under arbitrary wind loads.

# BIBLIOGRAPHY

Breuer, M. (1998). Large eddy simulation of the subcritical flow past a circular cylinder: numerical and modeling aspects. *International Journal for Numerical Methods in Fluids*, 28(9):1281–1302.

Breuer, M. (2000). A challenging test case for large eddy simulation: high reynolds number circular cylinder flow. *International Journal of Heat and Fluid Flow*, 21(5):648–654.

Catalano, P., Wang, M., Iaccarino, G., and Moin, P. (2003). Numerical simulation of the flow around a circular cylinder at high reynolds numbers. *International Journal of Heat and Fluid Flow*, 24(4):463–469.

Cheng, S., Irwin, P., Jakobsen, J., Lankin, J., Larose, G., Savage, M., Tanaka, H., and Zurell, C. (2003). Divergent motion of cables exposed to skewed wind. In *Proceedings of the 5th International Symposium on Cable Dynamics*, pages 271–278.

Cigada, A., Diana, G., Falco, M., Fossati, F., and Manenti, A. (1997). Vortex shedding and wake-induced vibrations in single and bundle cables. *Journal of Wind Engineering and Industrial Aerodynamics*, 72:253–263.

Davenport, A. (1995). The dynamics of cables in wind. In *Proceedings of Symposium on Cable Dynamics*.

Davis, D., Richards, D., and Scriven, R. (1963). Investigation of conductor oscillation on the 275 kv crossing over the rivers severn and wye. In *Proceedings of the Institution of Electrical Engineers*, volume 110, pages 205–219. IET.

Davison, A. (1930). Dancing conductors. *Transactions of the American Institute of Electrical Engineers*, 49(4):1444–1449.

Den Hartog, J. (1932). Transmission line vibration due to sleet. *Transactions of the American Institute of Electrical Engineers*, 51(4):1074–1076.

Den Hartog, J. P. (1985). *Mechanical vibrations*. Courier Corporation.

Dong, S. and Karniadakis, G. E. (2005). Dns of flow past a stationary and oscillating cylinder at. *Journal of Fluids and Structures*, 20(4):519–531.

Hikami, Y. and Shiraishi, N. (1988). Rain-wind induced vibrations of cables stayed bridges. *Journal of wind engineering and industrial aerodynamics*, 29(1):409–418.

Honda, A., Yamanaka, T., Fujiwara, T., and Saito, T. (1995). Wind tunnel tests on rain-induced vibration on the stay-cable. In *Proc Int Symp Cable Dynamics*, pages 255–262.

Irwin, P. A. (1997). Wind vibrations of cables on cable-stayed bridges. In *Building to Last:*, pages 383–387. ASCE.

Karman, T. v. and Sears, W. R. (1938). Airfoil theory for non-uniform motion. *Journal of the Aeronautical Sciences*, 5(10):379–390.

Kravchenko, A. G. and Moin, P. (2000). Numerical studies of flow over a circular cylinder at re d= 3900. *Physics of fluids*, 12(2):403–417.

Kumarasena, S., Jones, N. P., Irwin, P., and Taylor, P. (2005). Wind induced vibration of stay cables. Technical report.

Matsumoto, M., Saitoh, T., Kitazawa, M., Shirato, H., and Nishizaki, T. (1995). Response characteristics of rain-wind induced vibration of stay-cables of cable-stayed bridges. *Journal of Wind Engineering and Industrial Aerodynamics*, 57(2):323–333.

Matsumoto, M., Shiraishi, N., Kitazawa, M., Knisely, C., Shirato, H., Kim, Y., and Tsujii, M. (1990). Aerodynamic behavior of inclined circular cylinders-cable aerodynamics. *Journal of Wind Engineering and Industrial Aerodynamics*, 33(1-2):63–72.

Matsumoto, M., Yagi, T., Hatsuda, H., Shima, T., Tanaka, M., and Naito, H. (2010). Dry galloping characteristics and its mechanism of inclined/yawed cables. *Journal of Wind Engineering and Industrial Aerodynamics*, 98(6):317–327.

Norberg, C. (2013). Pressure forces on a circular cylinder in cross flow. In *IUTAM Symposium on Bluff Body Wakes, Dynamics and Instabilities, eds H Eckelmann, JMR Graham, P Hierre, PA Monkewitz*, pages 275–278.

Phelan, R. S., Sarkar, P. P., and Mehta, K. C. (2006). Full-scale measurements to investigate rain–wind induced cable-stay vibration and its mitigation. *Journal of Bridge Engineering*, 11(3):293–304.

Pontaza, J. P., Menon, R. G., and Chen, H.-C. (2009). Three-dimensional numerical simulations of flows past smooth and rough/bare and helically straked circular cylinders allowed to undergo two degree-of-freedom motions. *Journal of Offshore Mechanics and Arctic Engineering*, 131(2):021301.

Rawlins, C. (1981). Analysis of conductor galloping field observations-single conductors. *IEEE Transactions on Power Apparatus and Systems*, (8):3744–3753.

Roshko, A. (1961). Experiments on the flow past a circular cylinder at very high reynolds number. *Journal of Fluid Mechanics*, 10(03):345–356.

Sarkar, P., Mehta, K., Gardner, T., and Zhao, Z. (1998). Aerodynamic solutions to cable vibrations. In *Proc., Texas Section ASCE Fall 1998 Meeting*. ASCE.

Sarkar, P. P. and Gardner, T. B. (2000). Model tests to study rain/wind-induced vibration of stay cables. In *Advanced Technology in Structural Engineering*, pages 1–8.

Spalart, P., Jou, W., Strelets, M., Allmaras, S., et al. (1997). Comments on the feasibility of les for wings, and on a hybrid rans/les approach. *Advances in DNS/LES*, 1:4–8.

Travin, A., Shur, M., Strelets, M., and Spalart, P. (2000). Detached-eddy simulations past a circular cylinder. *Flow, Turbulence and Combustion*, 63(1-4):293–313.

Yeo, D., Jones, N., and Meneveau, C. (2007). Characteristics of aerodynamic forces on a cylinder at different yaw and inclination angles under flow at high reynolds number. In *Proceedings of the 12th International Conference of Wind Engineering, Cairns, Australia*, pages 879–886.

Yeo, D. and Jones, N. P. (2008). Investigation on 3-d characteristics of flow around a yawed and inclined circular cylinder. *Journal of Wind Engineering and Industrial Aerodynamics*, 96(10):1947–1960.

Yeo, D. and Jones, N. P. (2011). Computational study on aerodynamic mitigation of wind-induced, large-amplitude vibrations of stay cables with strakes. *Journal of Wind Engineering and Industrial Aerodynamics*, 99(4):389–399.

Yeo, D. and Jones, N. P. (2012). Aerodynamic forces induced by vertically oscillating incoming flow on a yawed horizontal circular cylinder. *Journal of Wind Engineering and Industrial Aerodynamics*, 104:188–195.

Yin, Z., Reddy, K., and Durbin, P. A. (2015). On the dynamic computation of the model constant in delayed detached eddy simulation. *Physics of Fluids*, 27(2):025105.

Yoshimura, T., Savage, M., Tanaka, H., and Urano, D. (1995). Wind-induced oscillations of groups of bridge stay-cables. *Journal of wind engineering and industrial aerodynamics*, 54:251–262.

Yukino, T., Fujii, K., and Hayase, I. (1995). Galloping phenomena of large bundle conductors observed on the full-scale test line. In *Proceeding of International Symposium on Cable Dynamics*, pages 557–563.

Zdravkovich, M. M. (2003). *Flow around Circular Cylinders: Volume 2: Applications*, volume 2. Oxford university press.

Zhao, M., Cheng, L., and Zhou, T. (2009). Direct numerical simulation of three-dimensional flow past a yawed circular cylinder of infinite length. *Journal of Fluids and Structures*, 25(5):831–847.